Physica B 663 (2023) 414981

Contents lists available at ScienceDirect

Physica B: Condensed Matter

journal homepage: www.elsevier.com/locate/physb

# Interconversion between dual-peak electromagnetically induced transparency and dual-peak electromagnetically induced absorption utilizing metasurface

You Lv [a], Di-Di Zhu [a], Tian-Qi Zhu [a], Jian-Yu Gong [b], Hai-Feng Zhang [a,*]

[a] College of Electronic and Optical Engineering & College of Flexible Electronics (Future Technology), Nanjing, 210023, PR China
[b] Portland Institute, Nanjing University of Posts and Telecommunications, Nanjing, 210023, PR China

ARTICLE INFO

*Keywords:*
Metasurface
Electromagnetically induced transparency
Electromagnetically induced absorption
Vanadium dioxide
Silicon

ABSTRACT

Utilizing metasurface (MS), the transition between dual-peak electromagnetically induced transparency (EIT) and dual-peak electromagnetically induced absorption (EIA) in four states has been proposed in the terahertz (THz) band with the incidence of a circularly polarized (CP) wave. Additionally, the phase-change material vanadium dioxide ($VO_2$) and photosensitive material silicon (Si) have been adopted. The four state transitions can be achieved by adjusting the pump light and the temperature which is not affected by incident CP waves. With the incidence of the pump light, Si can transform from the insulating state to the metallic state. Similarly, when the temperature exceeds 68 °C, $VO_2$ enters the metallic state. Two different dual-peak EIT (State 1 and State 2) accompanied by slow light effect can be observed by modulating the state of $VO_2$ without the action of Si. However, once Si is in metallic state, two different states of dual-peak EIA (State 3 and State 4) are achieved by changing the state of $VO_2$. Notably, the MS has the property of polarization insensitivity. The theoretical oscillator model and equivalent RLC-circuit model verify the feasibility of dual-peak EIT and EIA.

## 1. Introduction

The metasurfaces (MSs) [1] have got extensive attention due to their superior electromagnetic properties. Compared with 1D surfaces [2,3], they embrace more controllable dimensions. With the development of science and technology, MSs have good applications in photon deceleration and storage [4,5] and pulse regulation [6]. Terahertz (THz) waves refer to electromagnetic waves with wavelengths varying from 30 μm to 3000 μm and frequencies ranging from 0.1 THz to 10 THz [7]. The THz band was only proposed in the last decade and has rapidly developed as a global research hotspot due to its excellent electromagnetic properties [8,9]. At present, THz technology is widespread in spectroscopy [10–12], spin dynamics control [13,14], and multi-channel communication [15].

Electromagnetically induced transparency (EIT) is a quantum interference phenomenon in a three-atom energy level system [16]. It is the destructive interference between the transition channels of atoms due to incident electromagnetic waves, resulting in a high transmission window in the originally opaque absorption spectrum with a strong slow light effect and significant group delay. However, EIT phenomena in atomic systems are often realized in the laboratory and are always difficult to apply to devices. Fortunately, Zhang et al. successfully introduced EIT into the metamaterials in 2008 [17], making EIT has great potential value in nonlinearities [18], modulations, and slowing light propagation [19,20]. In the field of MSs, EIT is primarily created by the near-field interaction of bright and dark modes [21–23] and weak hybridization between bright and bright modes [24,25]. For the former, in contrast to the dark mode, which cannot directly couple the incident field's energy, the bright mode can be activated directly. However, the bright mode transfers energy to the dark mode through near-field coupling, thereby forming EIT [24,25]. For the latter, both bright modes can directly generate resonance by the incident field. Two bright modes form EIT by weak hybridization, which has been adopted in the proposed MS. On this basis, adding a resonator tends to form a dual-peak EIT. The resonator with the resonance frequency in the middle position is coupled with the other two resonators to form two high transmission windows, accompanied by two different group delays and slow light effects, which has great application prospects in multifunctional optical devices [26,27]. Owing to the rapid development of EIT, dual-band EIT has been suggested. Zhang et al. realized dual-mode EIT metamaterial

* Corresponding author. Nanjing University of Posts and Telecommunications (NJUPT) Nanjing, 210023, PR China.
*E-mail addresses:* hanlor@163.com, hanlor@njupt.edu.cn (H.-F. Zhang).

https://doi.org/10.1016/j.physb.2023.414981
Received 30 March 2023; Received in revised form 6 May 2023; Accepted 14 May 2023
Available online 17 May 2023

by using bright, quasi-dark, and dark mode resonators [28]. The dual-peak EIT in this work is established by the interactions between three metal resonators (demanding high requirements for suppressions of mutual interference between coupling paths).

Electromagnetically induced absorption (EIA) was first discovered in rubidium isotope atomic vapor by Lezama et al. in 1998 [29]. EIA is an interference phenomenon based on four atomic energy levels, which is a constructive interference phenomenon between the transition channels of atoms under the action of electromagnetic waves. EIA can produce a sharp absorption window in the otherwise transparent spectrum. In 2012, Sun et al. successfully realized EIA in the metamaterials with the phenomenon of accelerated group velocity [30]. Based on realizing EIT, EIA can be formed by reducing the dissipation loss of the bright mode, enhancing the dissipation loss of the dark mode, or reducing the coupling strength between the bright and dark modes by the formation of three-resonator systems [31,32]. The EIA is formed by the vertical coupling of three resonators [32]. Because of the narrow-band spectral characteristics of EIA, EIA has a wide range of applications in atomic clocks, atomic magnetometers, frequency stabilization of lasers, and the manipulation of light pulse speed [33–36]. Furthermore, the circular polarization (CP) wave has been considered in the paper. The CP waves can be categorized into the left-handed polarization (LCP) waves and right-handed polarization (RCP) waves. A large number of previous research works used linear polarization (LP) waves to excite MS-based EIT or EIA, so many devices and equipment related to EIT and EIA are limited to LP waves [37,38]. Compared with LP waves, CP waves have better stability and have been well used in invisibility cloaks [39–41], various lenses [42,43], and super-resolution imaging [44].

Additionally, the phase-change material $VO_2$ has been widely applied in the MS field [45–48]. Whenever the temperature is below 68 °C, $VO_2$ is in an insulating state, and the conductivity is 10 S/m [49]. Once the temperature surpasses 68 °C, the $VO_2$ transforms into a metallic state, and the conductivity can arrive at 300,000 S/m [49]. $VO_2$ plays an important role in a large number of smart devices that implement switchable and adjustable functions. In recent years, based on the phase-change properties of $VO_2$ from the insulating state to the metallic state, many tunable functional devices [50–52] have been developed. In addition to the phase change material $VO_2$, another material with variable properties, silicon (Si), is proposed in this paper [53,54]. The photosensitive material Si can be excited by the pump light, making it have metal-like properties with conductivity of 500,000 S/m [55]. When there is no pump light irradiation, Si is in an insulating state with the conductivity of 0 S/m [55]. Therefore, Si finds great applications in switchable reflectors/absorbers [56] and single-/single-band absorbers [57]. In this work, we only consider $VO_2$ conductivity in two states (0 and 300000 S/m). As a theoretical study, 68 °C is taken as the jump point between the two states while the introduction of external pump light does not cause the temperature to reach 68 °C and it is emphasized that VO2 and Si are two dielectric materials that do not affect each other.

In this paper, interconversion between dual-peak EIT and dual-peak EIA in four states utilizing phase-change material $VO_2$ and photosensitive material Si based on CP waves has been proposed from 0.2 THz to 1.2 THz in polarization-insensitive MS. By regulating pump light and temperature, dual-peak EIT and EIA can be switched in four states, and electromagnetic waves at different frequency bands can be selected according to demand. Separate dual-peak EIT and EIA effects have been studied by previous authors, but there is almost no integration of dual-peak EIT and EIA into a single device, let alone four states. This multifunctional integrator has great potential applications in the field of optical switching.

## 2. Modeling and design

### 2.1. Structure design

The overall structure's stereoscopic perspective and each layer's schematic diagram have been presented in Fig. 1d and e. It can be seen from Fig. 1e that there are five layers in this structure, which are three metal circular ring resonators and two Si resonators. The side length of the cell structure is $p = 150$ μm. The three metal circular rings are made of gold with a conductivity of $4.561 \times 10^7$ S/m [58]. The metal circular rings are defined as CR1, CR2, and CR3 from small to large, and the corresponding outer radii are $r_1$, $r_3$, and $r_5$, and the corresponding inner radii are $r_2$, $r_4$, and $r_6$, respectively as exhibited in Fig. 1a. The thickness of all gold resonators is 0.2 μm. Fig. 1b shows the parameters of four small Si square rings (SSRs) and one large Si square ring (LSR). The thicknesses of SSRs and LSRs are 0.7 μm and 0.5 μm respectively. Besides, the thickness parameters of each dielectric plate are shown in Fig. 1c. The lowermost dielectric substrate has a thickness of $h = 10$ μm and is composed of quartz [59]. The angles between the branches of $VO_2$ are $\theta_1 = \theta_3 = 22.5°$ and $\theta_2 = 45°$. $t_1$, $t_3$, $t_5$ represent the widths of the branches of $VO_2$ of CR1, CR2 and CR3, while $t_2$, $t_4$, $t_6$ are the lengths of the branches of CR1, CR2 and CR3. $h_i$ ($i = 1, 2, 3, 4, 5$) means the thickness of each layer of media from the bottom to the top as shown in Fig. 1c. Besides, $a$ and $b$ refer to the outer edge lengths of LSR and SSR respectively while $w$ and $w_1$ express the difference between the inner and outer edge lengths of LSR and SSR. All other dielectric spacers are made of Polymethylmethacrylate (PMMA) [60] which is a transparent organic glass with a dielectric constant of $\varepsilon = 2.5$. The stereoscopic view of the arrangement of the presented MS has shown in Fig. 1f. The specific parameters can be seen in Table 1. As is displayed in Fig. 2, when both $VO_2$ and Si are in an insulating state, it is the first dual-peak EIT state (State 1). A dual-peak EIT in another frequency band (State 2) can be achieved with the metallic state of only $VO_2$. The dual-peak EIT transforms into the dual-peak EIA of the first state (State 3) under the sole action of Si. Likewise, a second dual-peak EIA (State 4) is produced when $VO_2$ and Si are in a metallic state simultaneously. The operation concrete condition of different states has exhibited in Table 2. The proposed MS is simulated in the software HFSS. Multilayer structures can be fabricated by various techniques including the Langmuir-Blodgett method, sol-gel synthesis, electrochemical deposition, and chemical vapor deposition [61,62]. We can create heterolayered structures using the majority of these methods and regulate the thickness of each layer.

### 2.2. The study of dual-peak EIT

Currently, Fig. 3 shows the transmission curves and electric field distribution of CR3. When the temperature is lower than 68 °C, $VO_2$ is in an insulating state with the conductivity $n = 10$ S/m. CR3 can be considered a bright mode because CR3 can be directly excited at 0.516 THz and generate resonance at this time. As exhibited in Fig. 3c, the areas of the top left and lower right are where the electric field is most dense. When the temperature exceeds 68 °C, $VO_2$ branches change from the original insulating state to the metallic state, resulting in a shift in the geometry of CRs. And the resonance frequency of CR3 has a red-shift to 0.474 THz, and the transmission response is shown in Fig. 3a. At this time, the electric field distribution position of CR3 is not much different, and $VO_2$ can localize a part of the energy. Figs. 4 and 5 also show the distributions of the electric field and transmission responses of CR1 and CR2. When $n = 10$ S/m (300,000 S/m), CR1 and CR2 generate resonances at 1.201 (1.070) THz and 0.923 (0.757) THz. As shown in Fig. 4c, d, 5c, and 5d, the electric field distribution positions of CR1 and CR2 are similar to those of CR3. Since these three CRs can be directly excited by the incident field, they are all bright modes. As shown in Figs. 3b, 4b and 5b, different states of CRs can be freely adjusted by changing the outside temperature.

To observe the dual-peak EIT phenomenon, three CRs are put together. At this time, both LSR and SSRs are in this unit cell, but they do not come to function. For the convenience of understanding, LSR and SSRs are not shown in the following figures. CR2 and CR1, CR3 can be coupled separately to form coherent cancellation, resulting in the appearance of dual-peak EIT. The transmission response of State 1 is

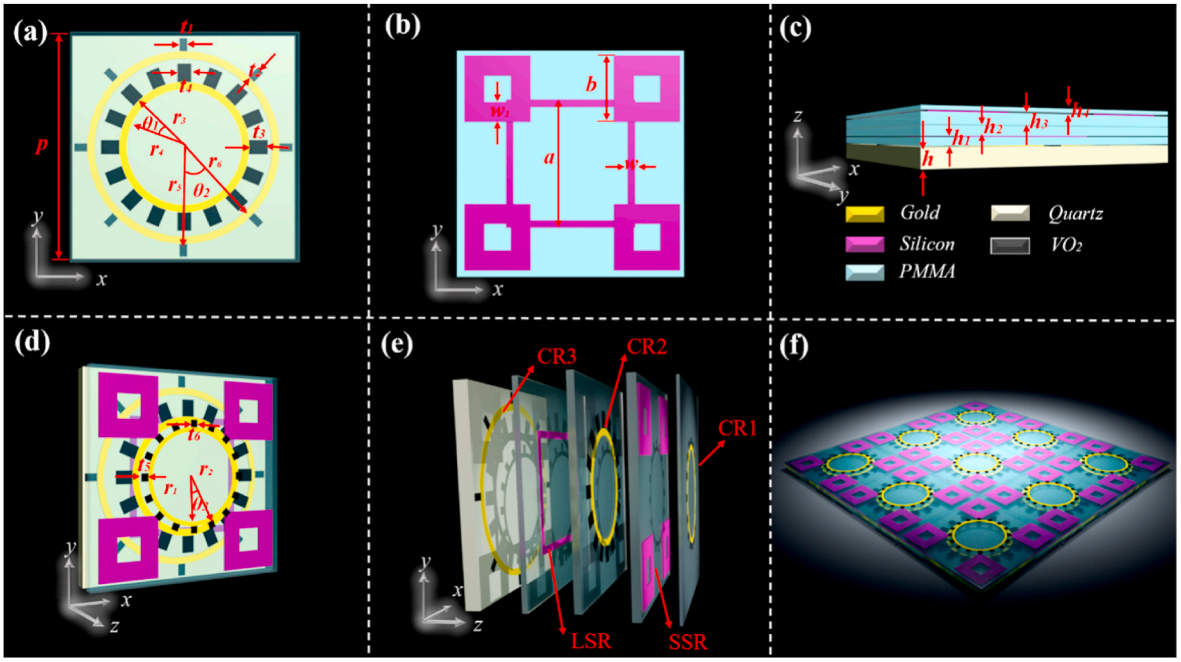


**Fig. 1.** (a) The top view of the CRs on the lower level, (b) the top view of Si resonators, (c) the side view of the proposed structure, (d) the stereoscopic view of the proposed overall structure, (e) schematic diagram of each layer structure, and (f) the stereoscopic view of the arrangement of the presented MS.

**Table 1**
The detailed values of various parameters in the presented MS.

| Parameters | Values (μm) | Parameters | Values (μm) | Parameters | Values (μm) |
|---|---|---|---|---|---|
| $h_1$ | 4 | $r_1$ | 35 | $w_1$ | 13 |
| $h_2$ | 5 | $r_2$ | 32 | $t_1$ | 5 |
| $h_3$ | 6 | $r_3$ | 43 | $t_2$ | 8.5 |
| $h_4$ | 2 | $r_4$ | 38 | $t_3$ | 12 |
| $h$ | 10 | $r_5$ | 65 | $t_4$ | 9 |
| $a$ | 85 | $r_6$ | 60 | $t_5$ | 5 |
| $b$ | 43 | $w$ | 5 | $t_6$ | 5 |

shown in Fig. 6. Two transparent windows at 0.482 THz-0.840 THz and 0.840 THz-1.239 THz have formed in the MS. The corresponding transmission dips are 0.029, 0.076, and 0.049, which are all below 0.1. The two peaks of State 1 are 0.917 and 0.847, and the corresponding frequencies are 0.622 THz and 0.964 THz. Besides, it can be seen in Fig. 6 that two transparent windows of State 2 are formed between 0.414 THz and 0.686 THz and 0.686 THz-1.091 THz. The highest transmission peaks at 0.482 THz and 0.835 THz are 0.728 and 0.760. The corresponding three transmission dips are 0.080, 0.093, and 0.084, all below 0.1. It is obvious from Fig. 6 that two states can transform into each other by heating and cooling process. When $VO_2$ is in the metallic state, all the branches of the circular resonator play a role. The parasitic capacitance can be generated between the branches, increasing the

**Table 2**
The operation concrete condition of different states.

| | State 1 | State 2 | State 3 | State 4 |
|---|---|---|---|---|
| Pump light | × | × | ✓ | ✓ |
| Heating | × | ✓ | × | ✓ |

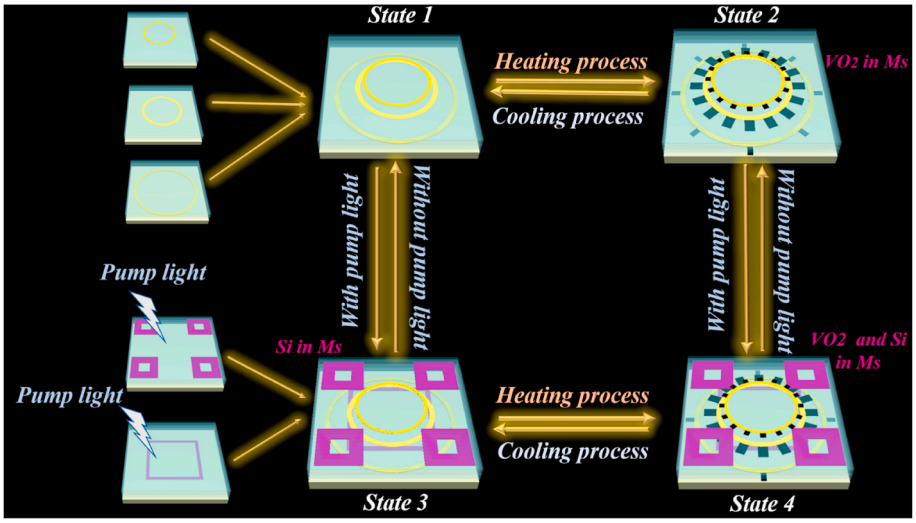


**Fig. 2.** The operational process of the proposed MS.

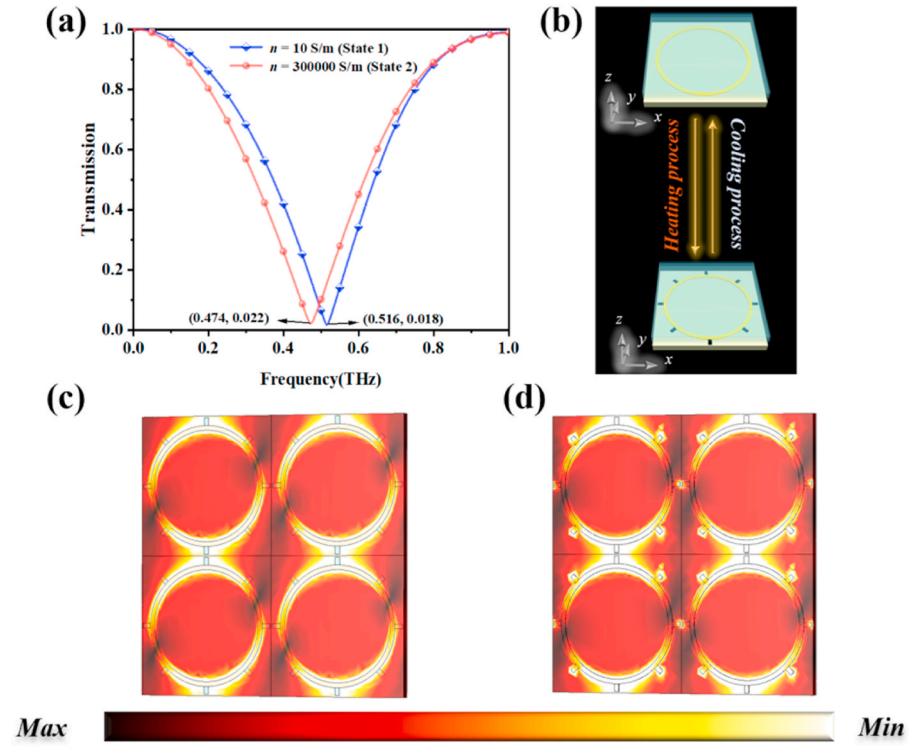


**Fig. 3.** a) The transmission curves of CR3 with the incidence of the LCP waves when $n = 10$ S/m and 300,000 S/m, b) the transition methods between two states, c) the electric field distribution of CR3 at 0.516 THz when $n = 10$ S/m, and d) at 0.474 THz when $n = 300{,}000$ S/m.

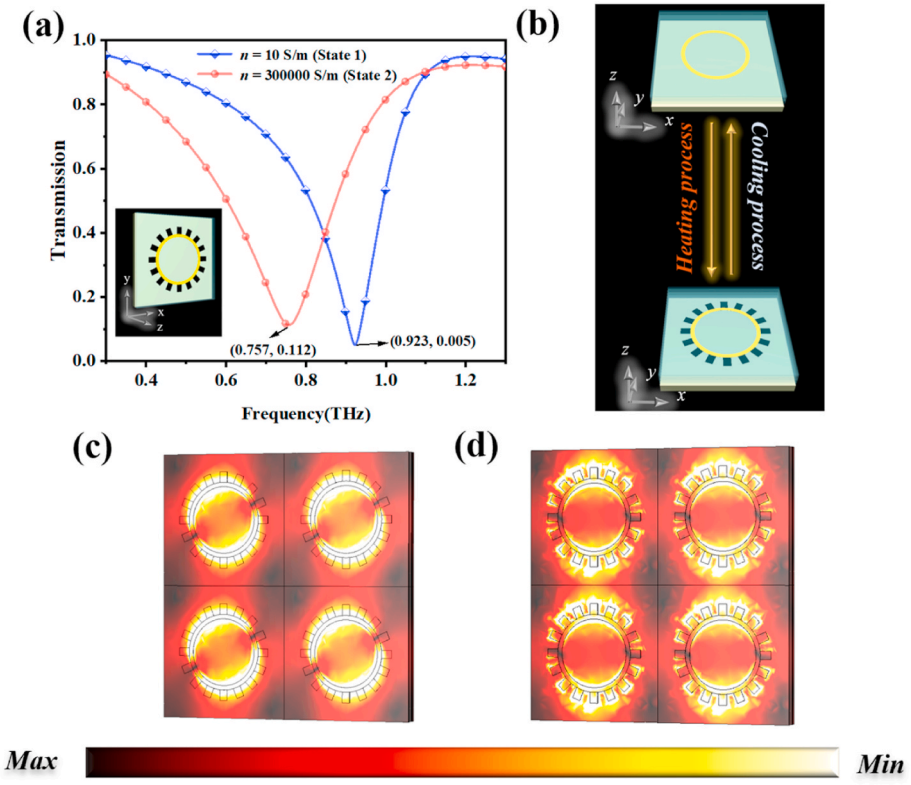


**Fig. 4.** a) The transmission responses of CR2 for the LCP waves when $n$ is 10 S/m and 300,000 S/m, b) the transition process between State 1 and State 2, c) the electric field distribution at 0.923 THz when $n = 10$ S/m and d) at 0.757 THz when $n = 300{,}000$ S/m.

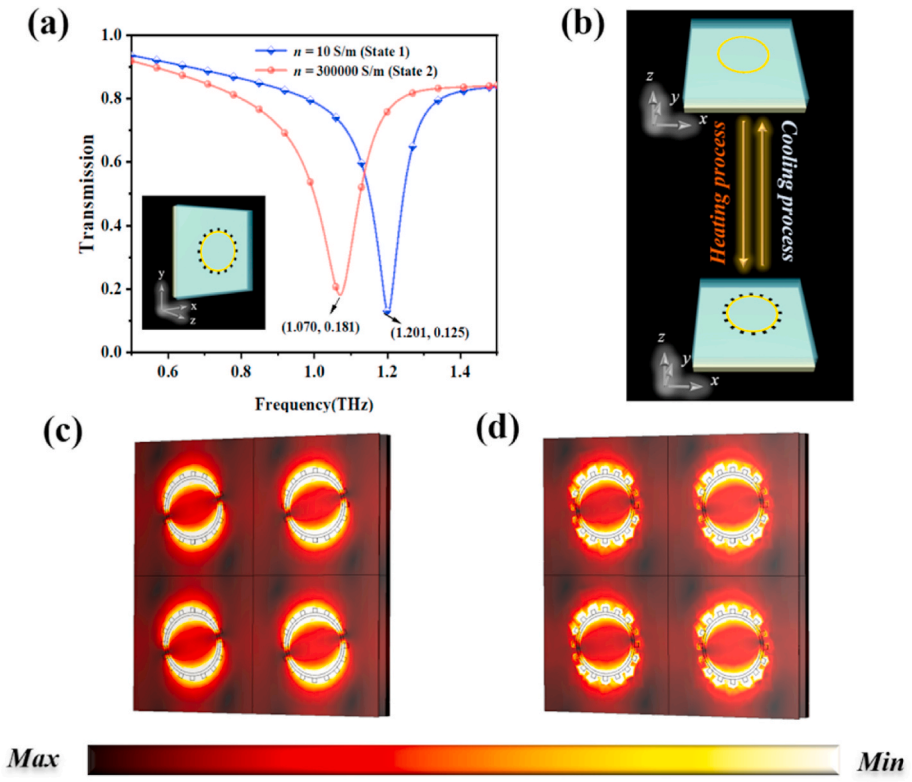


**Fig. 5.** a) The transmission responses of CR1 with $n = 10$ S/m and 300,000 S/m, b) the process of the transformation of two states, c) the electric field distribution at 1.201 THz when $n = 10$ S/m, and d) the electric field distribution at 1.070 THz with $n = 300{,}000$ S/m.

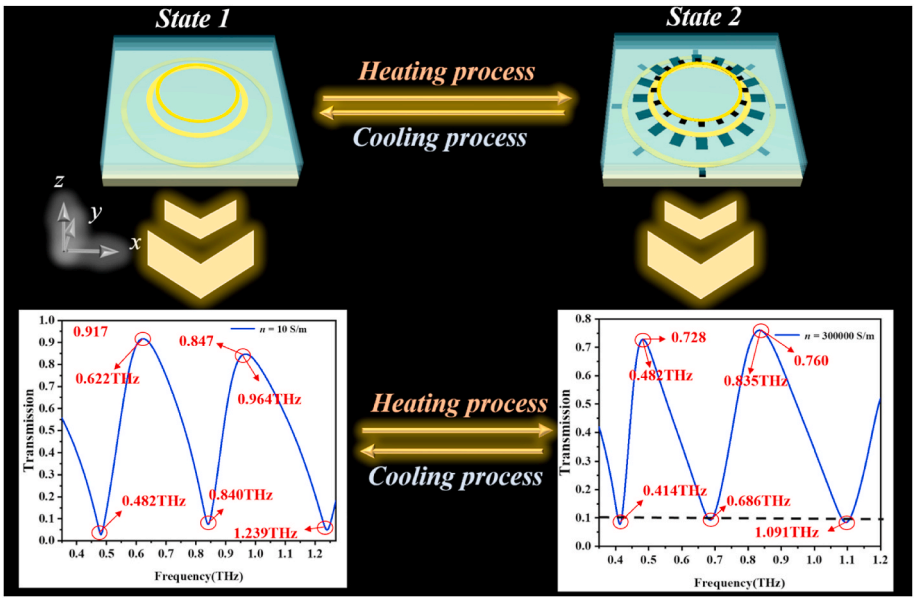


**Fig. 6.** Schematic diagram of the transition between the two states and the corresponding transmission curves.

equivalent capacitance of each resonator, while the equivalent inductance is almost constant. The formula for calculating the resonant frequency is as follows [63]:

$$f = \frac{1}{2\pi\sqrt{LC}} \tag{1}$$

According to the formula, it can be concluded that the resonant frequencies of circular resonators become smaller, and thus the red-shift phenomenon of transmission dip occurs, forming the different states of dual-peak EIT.

To better understand the principle of dual-peak EIT, the analysis is carried out from the perspective of surface current. When MS is in State 1, it can be seen from Fig. 7 that at $f = 0.482$ THz, the surface current of CR3 is strong, which is mainly concentrated in the upper right and lower left parts, while the surface current of CR1 and CR2 is extremely weak. Therefore, it can be understood that when $f = 0.482$ THz, only CR3 produces a strong current response, leading to the appearance of the transmission dip. The surface current of CR2 which is mainly focused in

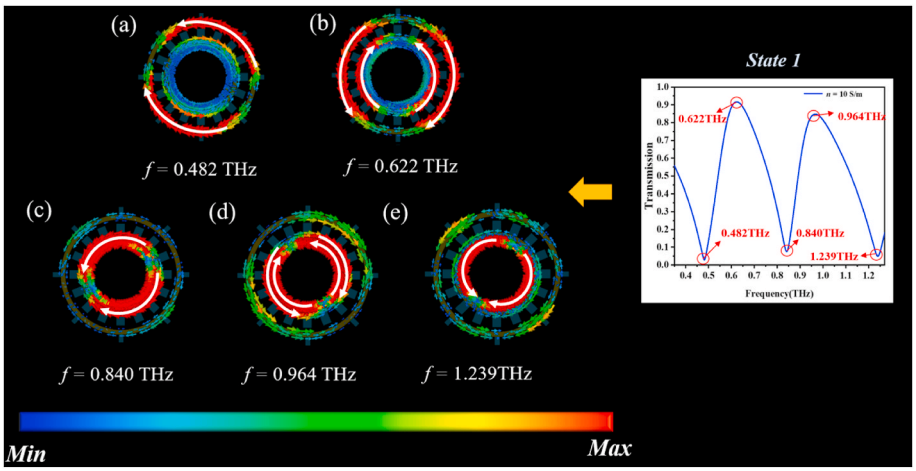


**Fig. 7.** The surface current distribution in State 1 at a) 0.482 THz, b) 0.622 THz, c) 0.840 THz, d) 0.964 THz, and e) 1,239 THz.

the upper left and lower right parts is significantly stronger than that of CR1 and CR3 at 0.840 THz, resulting in the second transmission dip. Similarly, when $f = 1.239$ THz, the third transmission dip occurs because the current response of MS is mainly generated by CR1, which is distributed at the upper left and lower right parts. As exhibited in Fig. 7b, both CR3 and CR2 can form resonance by the incident CP waves. Compared with $f = 0.482$ THz and $f = 0.840$ THz, the current distribution in CR3 and CR2 has been remarkably shifted at 0.622 THz. The current density has been enhanced and the current position has changed to the left and right sides. Since both CR3 and CR2 have a strong current response, they can be coupled with each other. As can be seen from Fig. 7c, the current directions on CR3 and CR2 are opposite, which leads to a stable phase difference between them. Therefore, there can be coherent cancellation between CR3 and CR2, leading to the appearance of destructive interference, thus forming EIT. When $f = 0.964$ THz, both CR2 and CR1 have a strong current response, but the direction of their surface current of them is opposite, resulting in the coherent cancellation between CR2 and CR1. Because of this, destructive interference has been generated, which can form EIT behavior. Hence, the dual-peak EIT has been generated in State 1 due to the destructive interference between CR3 and CR2 and between CR2 and CR1. Besides, when the MS is in State 2, the distribution of the current at different frequencies is consistent with State 1, and will not be described here. The current distributions at key frequencies are shown in Fig. 8. Therefore, the destructive interference between CR3 and CR2 and between CR2 and CR1 in State 2 has promoted the formation of the dual-peak EIT. Just as Fig. 6 displayed, States 1 and 2 can be adjusted by controlling the temperature outside.

In the transparency window of EIT, dramatic changes in phase lead to slow light effects with obvious group delay (GD). The slow light effect describes the slowing of the propagation of light. the GD of EIT can be reflected in MS. The corresponding calculation formula of GD are as follows [64]:

$$\tau_{GD} = -\frac{\partial \varphi}{\partial \omega} \tag{2}$$

where $\varphi$ and $\omega$ stand for the phase and the angular frequency, respectively. It can be seen from Fig. 9a–d that three drastic phase change has emerged in two transparency windows for dual-peak EIT in State 1 or State 2, which provides the conditions for the emergence of the slow light effect. As is revealed in Fig. 9b, in transparency windows of State 1, the maximum values of GD are 2.59 ps and 3.16 ps. Similarly, Fig. 9d have shown that the maximum values of GD are 4.13 ps and 2.52 ps in transparency windows of State 2. Since the proposed structure has two transparency states, there are four kinds of group velocities to choose from, which means that the MS has a promising future in controlling group velocities. It is a typical characteristic of EIT (the existence of GD), which indicates that the slow light effect can be applied to tunable slow light devices [65].

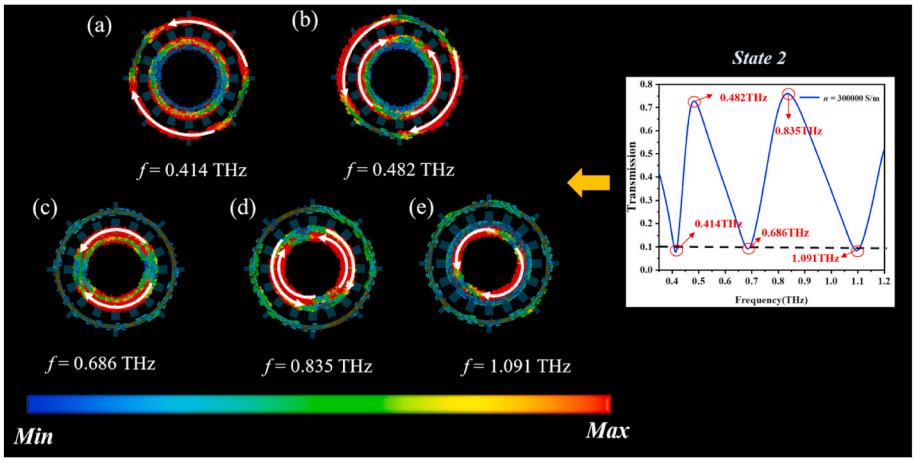


**Fig. 8.** The distribution of surface current in State 2 at a) 0.414 THz, b) 0.482 THz, c) 0.686 THz, d) 0.835 THz, and e) 1.091 THz.

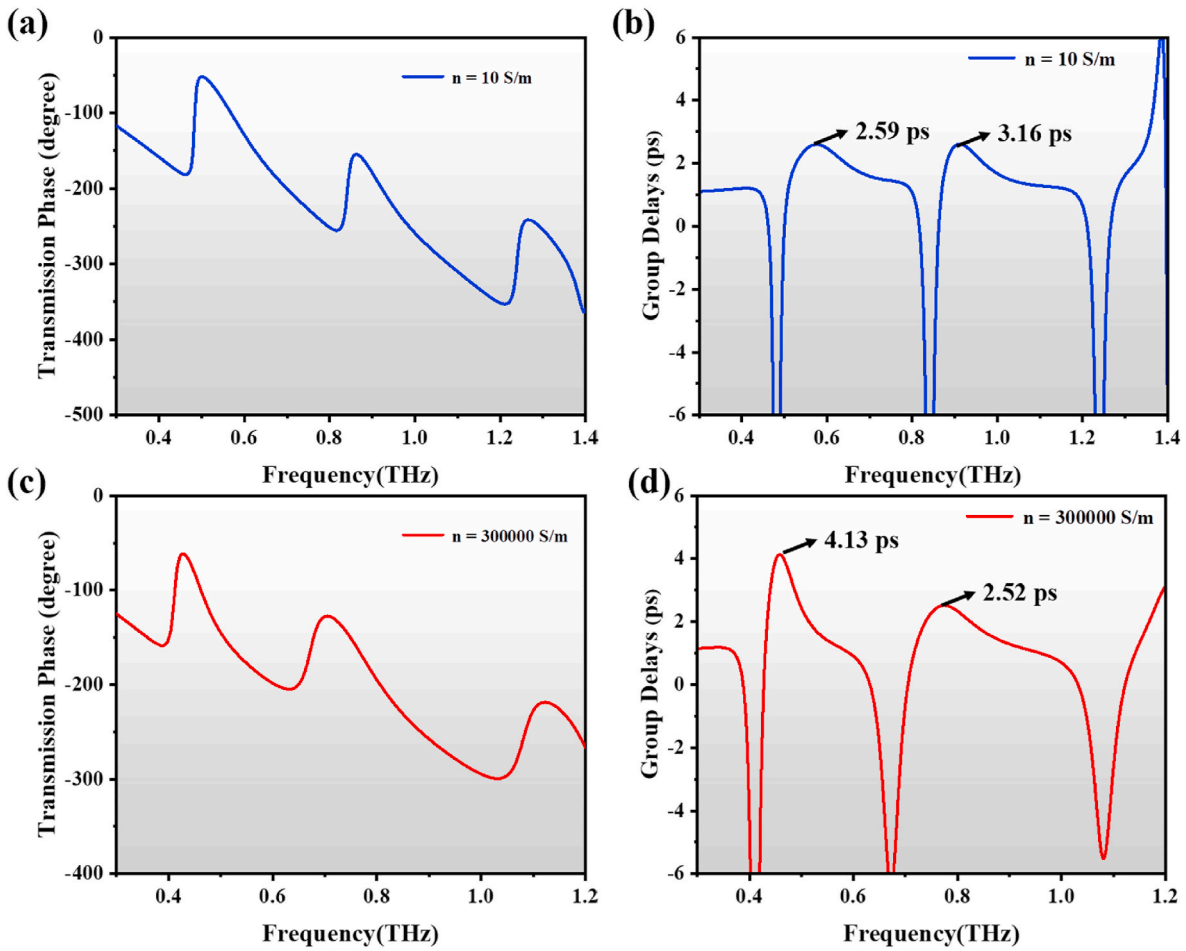


**Fig. 9.** a) The phase diagram, b) the GD for State 1, and c) the phase diagram, d) the GD for State 2.

### 2.3. *The study of dual-peak EIA*

When the proposed MS is irradiated with pump light, the conductivity of Si $k$ can gradually change from 0 S/m to 500,000 S/m [55]. When $k = 0$ S/m, both LSR and SSRs can be considered as not resonating as exhibited in the red transmission curves in Figs. 10 and 11. Whereby, the LSR and SSRs can be excited due to the existence of pump light. The transmission response has been revealed in Fig. 10a (bule curve), which indicates that LSR resonates at 0.724 THz and the corresponding value is 0.450. Fig. 10b clearly shows the electric field distribution at 0.724 THz. The upper left and lower right regions of LSR are heavily concentrated the electric field. Similarly, the transmission responses of SSRs are given in Fig. 11a (blue curve), where SSRs generate the resonance at 1.553 THz and the corresponding value is 0.346 THz. Besides, significant electric field energy exists near the SSRs as shown in Fig. 11b.

Currently, to study the phenomenon of dual-peak EIA behavior, CRs,

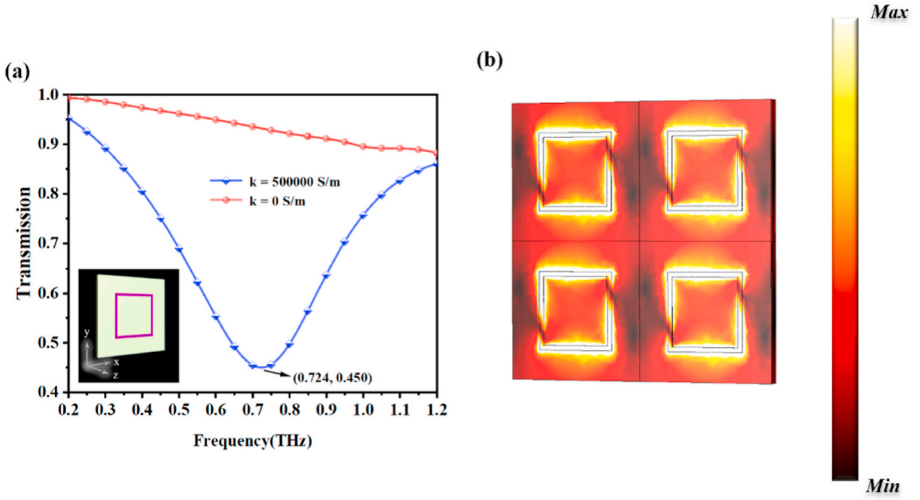


**Fig. 10.** a) The transmission curve of LSR, and b) the electric distribution of LSR for LCP waves with $k = 500{,}000$ S/m.

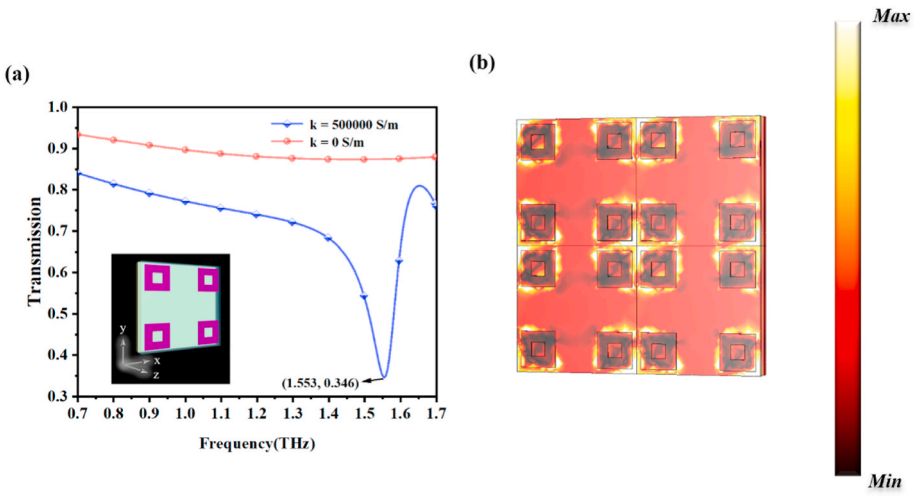


**Fig. 11.** a) The transmission response of SSRs, and b) the electric distribution of SSRs with the incidence of LCP waves with $k$ = 500,000 S/m.

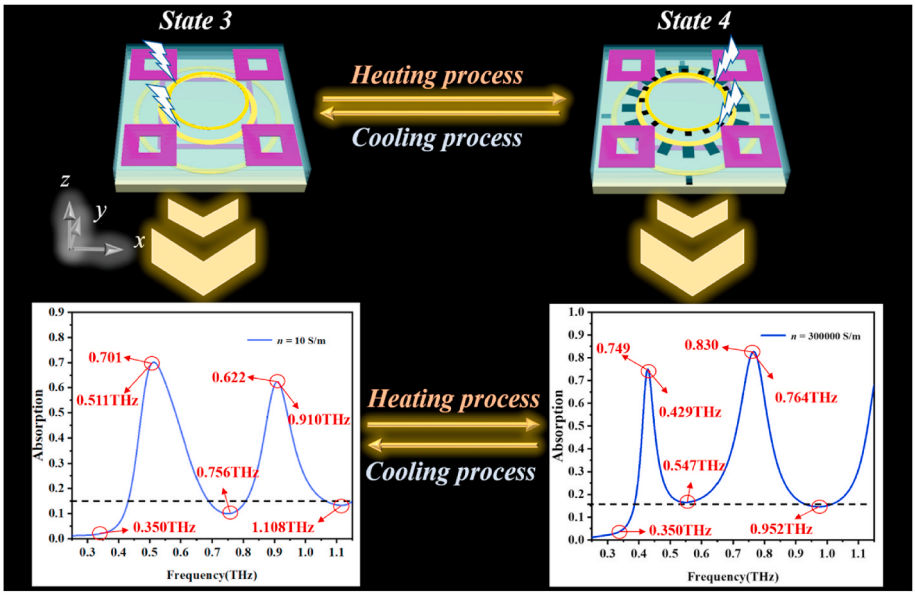


**Fig. 12.** Schematic diagram of the transition between State 3 and State 4 and the corresponding absorption curves with the incidence of pump light and LCP waves.

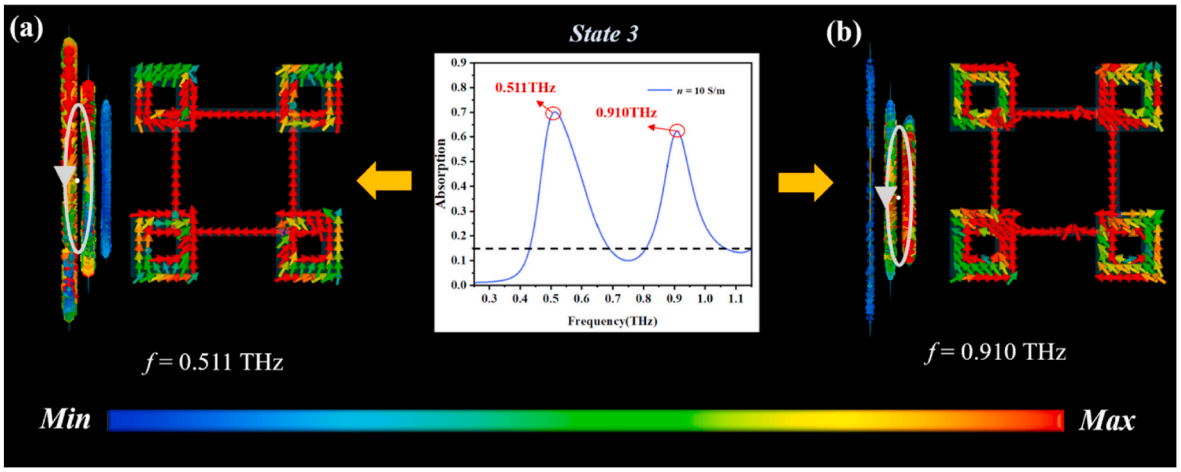


**Fig. 13.** Surface current distribution of metal resonators and displacement current distribution of Si resonators in State 3 at a) 0.511 THz, and b) 0.910 THz.

LSR, and SSRs are put together in one unit cell. When illuminated by pump light, the conductivity of Si $k$ can turn to 500,000 S/m. Therefore, the conversion of dual-peak EIT to dual-peak EIA can be realized just as revealed in Fig. 12. For the convenience of understanding below, we refer to the MS when Si is in the metallic state alone as State 3, and when Si and $VO_2$ act simultaneously as State 4. As shown in Fig. 12, it can be seen that two sharp absorption windows have formed in this MS at 0.350 THz-0.756 THz and 0.756 THz-1.108 THz in State 3, and the frequencies corresponding to the absorption peaks are 0.511 THz and 0.910 THz. The corresponding values of the three absorption dips are 0.022, 0.099, and 0.132 respectively. Meanwhile, the absorption rates at 0.511 THz and 0.910 THz can reach 0.701 and 0.622. When MS is in State 4, two absorption windows are achieved at 0.350 THz-0.547 THz and 0.547 THz-0.952 THz, and the peak frequencies are 0.429 THz and 0.764 THz. Similarly, the values of the three absorption dips are 0.048, 0.149, and 0.146. The absorption rates at the peak have reached 0.749 and 0.830. Fig. 12 shows how the two absorption states are designed and switched. LSR and SSRs can be successfully excited with the incidence of pump lights, resulting in the transition between transparency states and absorption states. And States 3 and 4 can be converted to each other through the heating process and cooling process.

Figs. 13 and 14 show the surface currents and displacement current at the peak absorption of each resonator in different absorption states with the incidence of pump light and LCP waves. LSRs and SSRs have strong current effects. As displayed in Fig. 13a for State 3, when LSRs and SSRs in the metallic state, the surface currents of CR3 and CR2 are enhanced while that of CR1 is weak and were able to form magnetic dipoles on the side. Similarly, under the action of LSRs and SSRs, CR3 and CR2 can also form magnetic dipoles at 0.429 THz as shown in Fig. 14a. Analogously, the magnetic dipoles could be generated by CR3 and CR2 at 0.910 THz for State 3 and 0.764 THz for State 4 in Figs. 13b–14b. The energy of the incident magnetic field can be effectively captured by the magnetic dipole, producing strong absorption, which leads to the transformation of the original destructive interference into constructive interference. It is obvious from Fig. 15 that the intrinsic absorption of the system is significantly stronger when $VO_2$ is in the metallic state ($n$ = 300,000 S/m) than when $VO_2$ is in the insulating state ($n$ = 0 S/m). Although the surface current at 0.910 THz in state 3 is stronger than 0.764 THz in state 4, the intrinsic absorption brought by the system in state 4 cancels out some of the current effects, resulting in absorption at 0.910 THz in state 3 weaker than the absorption effect at 0.764 THz in state 4. Hence, the original transparency window is converted into the current absorption window, and the dual-peak EIT is thus converted into another dual-peak EIA.

### 2.4. Atomic energy level theory

To better understand the formation principles of dual-peak EIT and dual-peak EIA, Fig. 16 provides a description of the atomic theory

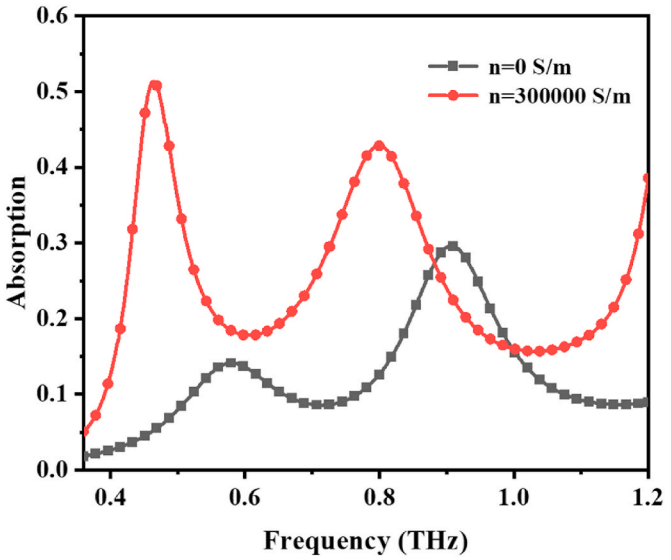


**Fig. 15.** MS intrinsic absorption curves of $VO_2$ in the insulating and metallic states, respectively, when Si is in the insulating state.

associated with EIT and EIA, where the $\Omega_i$ ($i$ = 1, 2, 3) refer to the transition phases, and the $C_i$ denote the coupling coefficients between energy levels. the three-level atomic transition model [66] is exhibited in Fig. 16a, where atoms transit from the ground state |1> to the excitation state |2> with the interaction of coupling light. With the incidence of a probing light stronger than the coupling light, atoms in the ground state |3> energy level leap, forming a |3>→|2> channel. Hence, a transparent window is occurred in quantum mechanics. The channels from |1> to |2> are occupied by CR1 and CR2 represents the process from |3> to |2>. The transparent window is observed under the induction electric field irradiation. Furthermore, with reference to Fig. 16b, the generation principle of dual-peak EITs is sketched, where an additional path from another energy level |4> to energy level |2> is built up by attaching a CR3 to the MS. The phase extinction interference induced by the interaction between the channels from |1> to state |2> and state |4> to state |2> will cause another transparent window. Therefore, dual-peak EIT can generate in atomic system.

For the purpose of realizing the self-modulation of the device, the Si resonators have to be added. With the irradiation of pump light, LSR and SSRs transform into a metallic state, which enhances the dissipation of metal resonator. When LSRs and SSRs are involved in the coupling, the damping factor of the circular resonator is thus changed, resulting in a modification of the phase of coupling channels. Constructive interference gradually overwhelms destructive interference and further gives rise to the formation of the absorption windows in original transparency

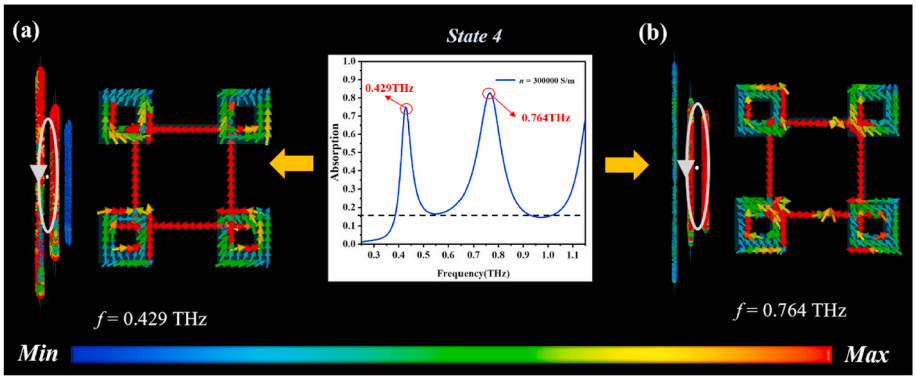


**Fig. 14.** Surface current distribution of metal resonators and displacement current distribution of Si resonators in State 4 at a) 0.429 THz, and b) 0.764 THz.

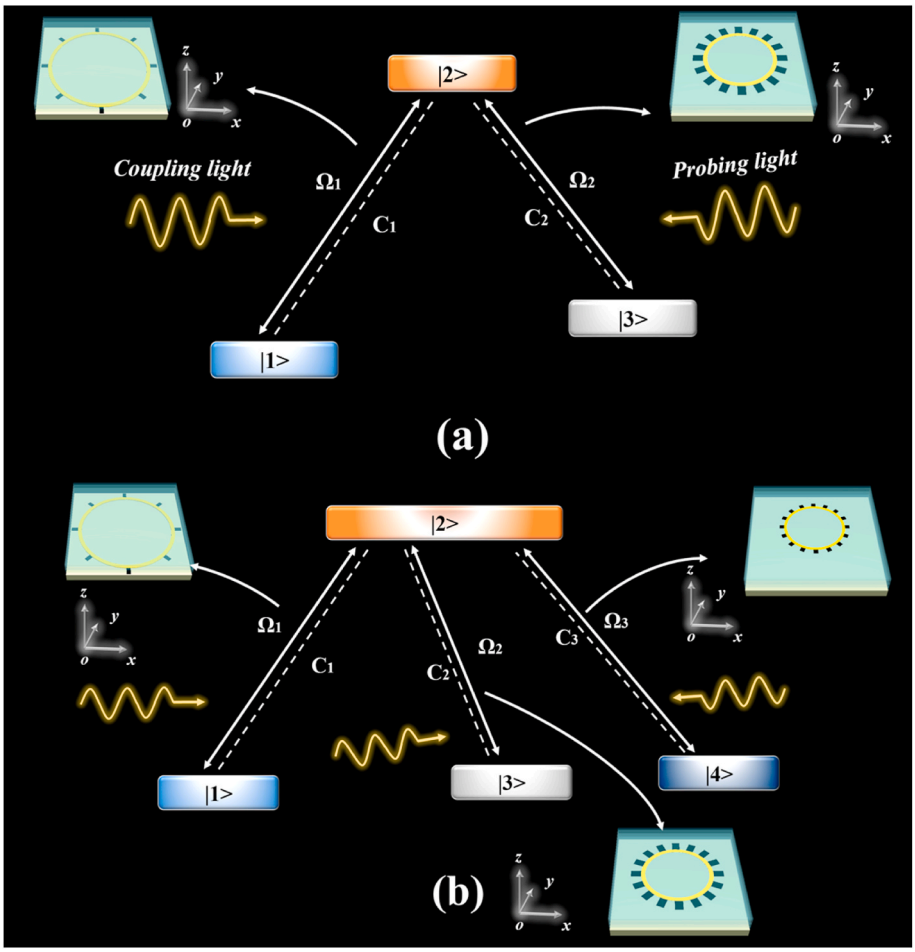


**Fig. 16.** The three-level system associated with EIT and EIA and its dual-peak extension, (a) classic three-level system in EIT and EIA MS, and (b) the expansion of EIT and EIA effects in multi-frequency.

windows. Therefore, the transition between dual-peak EIT to dual-peak EIA is achieved successfully.

## 3. Theoretical models of EIT and EIA effects

### 3.1. The analysis of RLC circuit model

Based on the theoretical discussion above, Fig. 17 demonstrates the thorough investigation of dual-peak EIT and EIA. The five resonators can be divided into two parts as displayed in Fig. 17a–b. The gold resonators and $VO_2$ branches are considered as Part 1. The equivalent circuit is shown in Fig. 17a, where $L_i$ ($i$ = 1, 2, 3) is the self-inductance of gold resonators, $C_i$ represents the gap capacitance between gold resonators and $R_i$ means the resistance of different metal resonators which makes great differences in the ohmic and radiation loss [67]. Since different resonators can be coupling with each other, the coupling capacitances

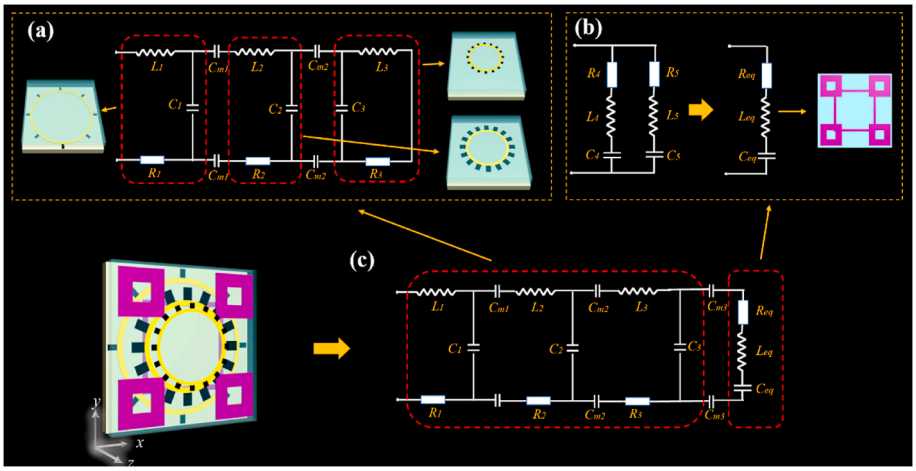


**Fig. 17.** a) The equivalent circuit model of dual-peak EIT, b) Si resonators, and c) the dual-peak EIA.

$C_{m1}$ and $C_{m2}$ are introduced into the circuit. By combining the three RLC loops, two destructive interferences can be easily formed in different frequencies resulting in the dual-peak EIT. Besides, two Si resonators can be also described as two RLC loops as displayed in Fig. 17b. Similarly, the self-inductance, gap capacitance, and resistance of LSR and SSRs are denoted by $L_4$, $C_4$, $R_4$, and $L_5$, $C_5$, $R_5$, respectively. Two RLC loops of LSR and SSRs can be equivalent to a new RLC loop which can be simplified by $L_{eq}$, $C_{eq}$, and $R_{eq}$. By gathering Part 1 and Part 2 together, the new circuit has generated in Fig. 17c, where $C_{m3}$ and $C_{m4}$ are used to reflect the coupling effect between metal resonators and Si resonators. Hence, constructive interference can be formed and further give rise to the dual-peak EIA in the circuit model in Fig. 17c.

Based on the discussion above, the corresponding circuit model [68] is used to certify the mechanism of dual-peak EIT and EIA just as shown in Fig. 18a. The EIT window in the multispectral response is a strong interference effect with the resonance detuning due to the relative spatial displacement of the positions of the open spectral bands. Different RLC values can be applied to an existing configuration when a new stub is introduced, corresponding to the three transmission dips of the dual-peak EIT. The stub can be swapped out for lumped energy to represent the detuning effect. Fig. 18a shows the equivalent RLC circuit based on the structure of this paper. A RLC loop represents an interference path or a resonator. Using the resonance between inductance and capacitance, the position of the resonance frequency of each resonator can be obtained, and the calculation formula is as shown in Equation [1], while the resistance $R$ mainly controls the current intensity in the loop, indicating the values of the transmission dips. Whereby, the interference effect between the three RLC resonators represents the interference between the three resonators of the dual-peak EIT, resulting in the formation of two destructive interferences in path 1 and path 2, path 2 and path 3. Path 1, path 2, and path 3 can be equivalent to CR3, CR2, and CR1 respectively as displayed in Fig. 18a. $Z_1$ and $Z_2$ represent the source impedance of the two ports and their values are both 50 Ω for EIT. The specific $R$, $L$, and $C$ values for different transparency states are listed in Tables 3 and 4. It can be apparently seen from Figs. 18b–c that there is a certain deviation between the simulated and analytically calculated curves which are more likely to result from the ignorance of the coupling capacitances between metal resonators. However, the simulated and analytically calculated curves basically coincide, illustrating the correctness and feasibility of the circuit model.

**Table 3**
The values of specific parameters of dual-peak EIT in State 1.

| Parameters | Values (Ω) | Parameters | Values (pH) | Parameters | Values (fF) |
|---|---|---|---|---|---|
| $R_1$ | 0.5 | $L_1$ | 15 | $C_1$ | 7.6 |
| $R_2$ | 1.8 | $L_2$ | 15 | $C_2$ | 2.35 |
| $R_3$ | 1 | $L_3$ | 4 | $C_3$ | 4 |

**Table 4**
The values of specific parameters of dual-peak EIT in State 2.

| Parameters | Values (Ω) | Parameters | Values (pH) | Parameters | Values (fF) |
|---|---|---|---|---|---|
| $R_1$ | 2 | $L_1$ | 16 | $C_1$ | 9.5 |
| $R_2$ | 2.39 | $L_2$ | 8 | $C_2$ | 6.8 |
| $R_3$ | 0.2 | $L_3$ | 3 | $C_3$ | 7 |

Dual-peak EIA can be also understood as the near-field coupling between multiple resonators with no detuning frequencies, which can be analogies to the RLC resonant circuit in Fig. 19a. As the increasing of RLC loops generated constructive interference gradually overwhelms the remaining effects of the destructive interference and finally results in the generation of two absorption windows in the original transparency

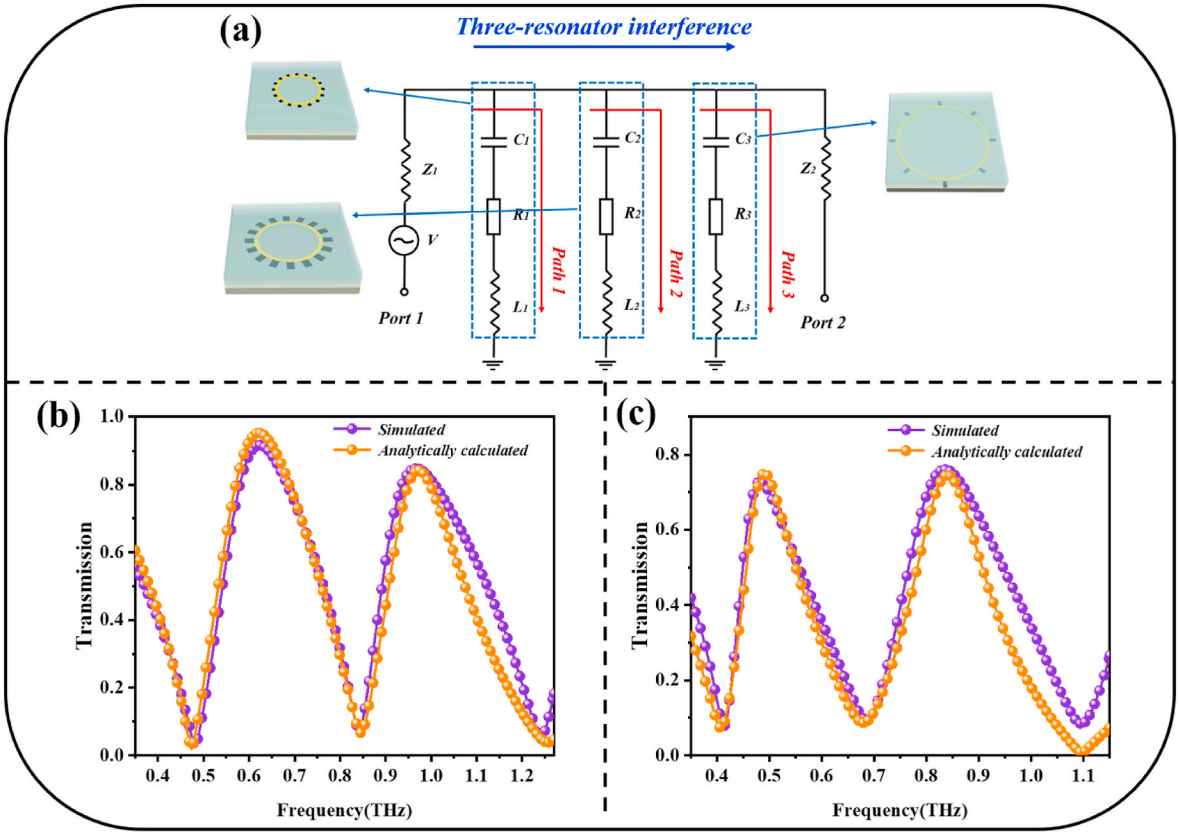


**Fig. 18.** (a) Equivalent circuit model with three connected RLC loops for dual-peak EIT, (b) the comparison of simulated and analytically calculated curves in State 1, and (c) in State 2.

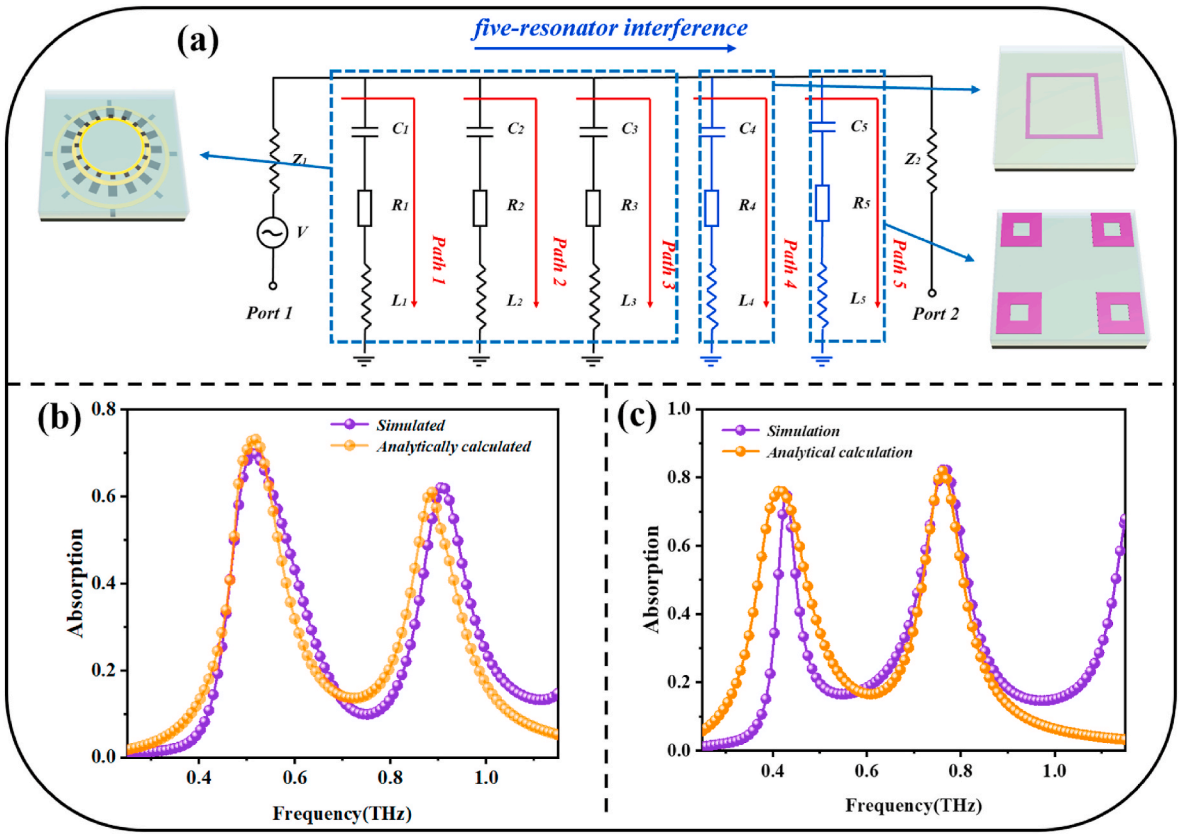


**Fig. 19.** a) Equivalent circuit model of dual-peak EIA based on five-resonator interference, b) the results of the comparison between simulated and analytically calculated curves in State 3, and c) in State 4.

windows. On basis of the RLC series resonant circuits in Fig. 19a, the existence of coupling capacitances leads to the bias of the simulated curves and analytically calculated curves in State 3 and State 4 as shown in Fig. 19b–c. Nevertheless, the high coincidence of the two curves confirms the correctness of the proposed MS. The values of the source impedance $Z_1$ and $Z_2$ in State 3 (4) are 4 Ω (4 Ω) and 20 Ω (19 Ω). Tables 5 and 6 have displayed every loop of $R_i$, $L_i$, $C_i$ ($i$ = 1, 2, 3, 4, 5) values.

### 3.2. The analysis of oscillator model

It is well known that both this type of dual-frequency EIT and EIA can be analyzed numerically with a three-particle model. The system can be represented by the following equation [69]:

$$\ddot{x}_1(t) + \gamma_1\dot{x}_1(t) + \omega_1^2 x_1(t) + \Omega_1^2 x_2(t) + \Omega_2^2 x_3(t) = Q_1 E \Big/ M_1 \tag{3}$$

$$\ddot{x}_2(t) + \gamma_2\dot{x}_2(t) + \omega_2^2 x_2(t) + \Omega_1^2 x_1(t) = Q_2 E \Big/ M_2 \tag{4}$$

**Table 5**
The values of specific parameters of dual-peak EIA in State 3.

| Parameters | Values (Ω) | Parameters | Values (pH) | Parameters | Values (fF) |
|---|---|---|---|---|---|
| $R_1$ | 7 | $L_1$ | 13 | $C_1$ | 7 |
| $R_2$ | 5 | $L_2$ | 15 | $C_2$ | 2.05 |
| $R_3$ | 1 | $L_3$ | 4 | $C_3$ | 1 |
| $R_4$ | 1 | $L_4$ | 20 | $C_4$ | 5.4 |
| $R_5$ | 1 | $L_5$ | 10 | $C_5$ | 3 |

**Table 6**
The values of specific parameters of dual-peak EIA in State 4.

| Parameters | Values (Ω) | Parameters | Values (pH) | Parameters | Values (fF) |
|---|---|---|---|---|---|
| $R_1$ | 30 | $L_1$ | 50 | $C_1$ | 2.6 |
| $R_2$ | 15 | $L_2$ | 40 | $C_2$ | 4 |
| $R_3$ | 20 | $L_3$ | 50 | $C_3$ | 0.84 |
| $R_4$ | 10 | $L_4$ | 20 | $C_4$ | 7 |
| $R_5$ | 5 | $L_5$ | 14 | $C_5$ | 3 |

$$\ddot{x}_3(t) + \gamma_3\dot{x}_3(t) + \omega_3^2 x_3(t) + \Omega_2^2 x_1(t) = Q_3 E \Big/ M_3 \tag{5}$$

Let labels 1, 2 and 3 represent the CR1, CR2 and CR3 resonators, respectively. In this case, $x_i$ (i = 1, 2, 3), $\omega_i$, and $\gamma_i$, are the respective displacements (having the complex form $x_i = x_i e^{j\omega t}$), the damping factor and the resonant frequency of the oscillator. the coupling strengths of CR2 to CR1 and CR2 to CR1 are denoted by the symbols $\Omega_1$ and $\Omega_2$, respectively. $M_i$ and $Q_i$ denote the effective charge and mass, respectively. $E = E_0 e^{j\omega t}$ is the incident electric field.

However, this three-oscillator coupling process is complex and tedious. It should be noted that a specific physical model is intended to numerically validate the resonance patterns and correlations we obtain in the simulations. In fact, the three-oscillator model can be further simplified. Suppose that the coupling between CR1 (oscillator 1) and CR2 (oscillator 2) is first generated, also giving rise to the typical EIT response. In this case, a new oscillator is defined to represent the state synthesis of oscillator 1 and oscillator 2, which then couples with CR3 (oscillator 3) to further generate the EIT response. Thus, the three-oscillator model can be condensed to a two-oscillator model, and the essence of generating EIT is unchanged, and different models are used to

find coupling correlations. In the two-oscillator model, the kinetic differential equation is expressed as [70,71]:

$$\ddot{x}_1(t) + \gamma_1\dot{x}_1(t) + \omega_0^2 x_1(t) + k^2 x_2(t) = g_1 E \tag{6}$$

$$\ddot{x}_2(t) + \gamma_2\dot{x}_2(t) + (\omega_0 + \delta)^2 x_2(t) + k^2 x_1(t) = g_2 E \tag{7}$$

where $\omega_0$ and $\omega_0 + \delta$ stand for the resonance frequencies of the two modes. $k$ and $\delta$ indicate the coupling coefficient and detuning factor between the two modes, while $g_1$ and $g_2$ represent the coupling strength between the resonator and the incident field. However, to better simplify the calculation, $g_2$ is usually considered to be zero due to the larger value of the Q-factor and less interaction with the incident field. The approximate relationship $\omega\text{-}\omega_0 \ll \omega_0$ can be transformed into $\omega_0^2\text{-}\omega^2 \approx -2\omega_0\,(\omega\text{-}\omega_0)$, which can be combined with Eqs. (7) and (8) to give the following formula [70,71]:

$$T = 1 - \mathrm{Re}\frac{ig_1{}^2(\omega - \omega_0 - \delta - i\gamma_2)}{(\omega - \omega_0 + i\gamma_1/2)(\omega - \omega_0 - \delta + i\gamma_2/2) - ik^2/4} \tag{8}$$

For state 1, the deduced fitting parameters are: $\omega_0 = 4.25$, $k = 0.03$, $\gamma_1 = 2.06$, $\gamma_2 = 1.00$ in the first window and $\omega_0 = 6.60$, $k = 0.037$, $\gamma_1 = 5.10$, $\gamma_2 = 2.00$ in the second window. For state 2, the deduced fitting parameters are: $\omega_0 = 3.50$, $k = 0.022$, $\gamma_1 = 2.01$, $\gamma_2 = 2.00$ in the first window and $\omega_0 = 5.70$, $k = 0.036$, $\gamma_1 = 5.10$, $\gamma_2 = 2.00$ in the second window. Fig. 20 illustrates the comparison between simulated curves and analytically calculated curves of oscillator models.

Additionally, if the coupling strength $k$ between two oscillators is treated as a real number like EIT, the model may violate the spectral characteristics of EIA. Therefore, a complex coupling parameter $ke^{i\varphi}$ has been implemented to accurately illustrate the EIA system, where the parameter $\varphi$ is the phase shift between the two oscillators caused by the delay effect of the coupling distance in the direction of propagation. It can be found that the model is only suitable for describing the EIT phenomenon when $\varphi = 0$, while when $\varphi = \pi/2$, it is only applicable for EIA resonance. Hence, by altering the value of $\varphi$, EIT to EIA conversion is possible. Other parameters have the same meaning as in EIT. The specific formula is as follows [70,71]:

$$\ddot{x}_1(t) + \gamma_1\dot{x}_1(t) + \omega_0^2 x_1(t) + ke^{i\varphi}x_2(t) = g_1 E(t) \tag{9}$$

$$\ddot{x}_2(t) + \gamma_2\dot{x}_2(t) + (\omega_0 + \delta)^2 x_2(t) + ke^{i\varphi}x_1(t) = g_2 E(t) \tag{10}$$

here using $x_1(t) = x_1e^{-i\omega t}$, $x_2(t) = x_2e^{-i\omega t}$ and $E_0(t) = E_0e^{-i\omega t}$ can get the absorption rate formula [70,71]:

$$A(\omega) = \mathrm{Re}\frac{ig_1{}^2(\omega - \omega_0 - \delta + i\gamma_2/2)}{(\omega - \omega_0 + i\gamma_1/2)(\omega - \omega_0 - \delta + i\gamma_2/2) - k^2e^{i2\varphi}/4} \tag{11}$$

hence, for state 3, the parameter values are: $\omega_0 = 3{,}24$, $k = 0.104$, $\gamma_1 = 0.90$, $\gamma_2 = 0.60$ in the first window and $\omega_0 = 5.74$, $k = 0.004$, $\gamma_1 = 0.70$, $\gamma_2 = 0.60$ in the second window. For state 4, the deduced fitting

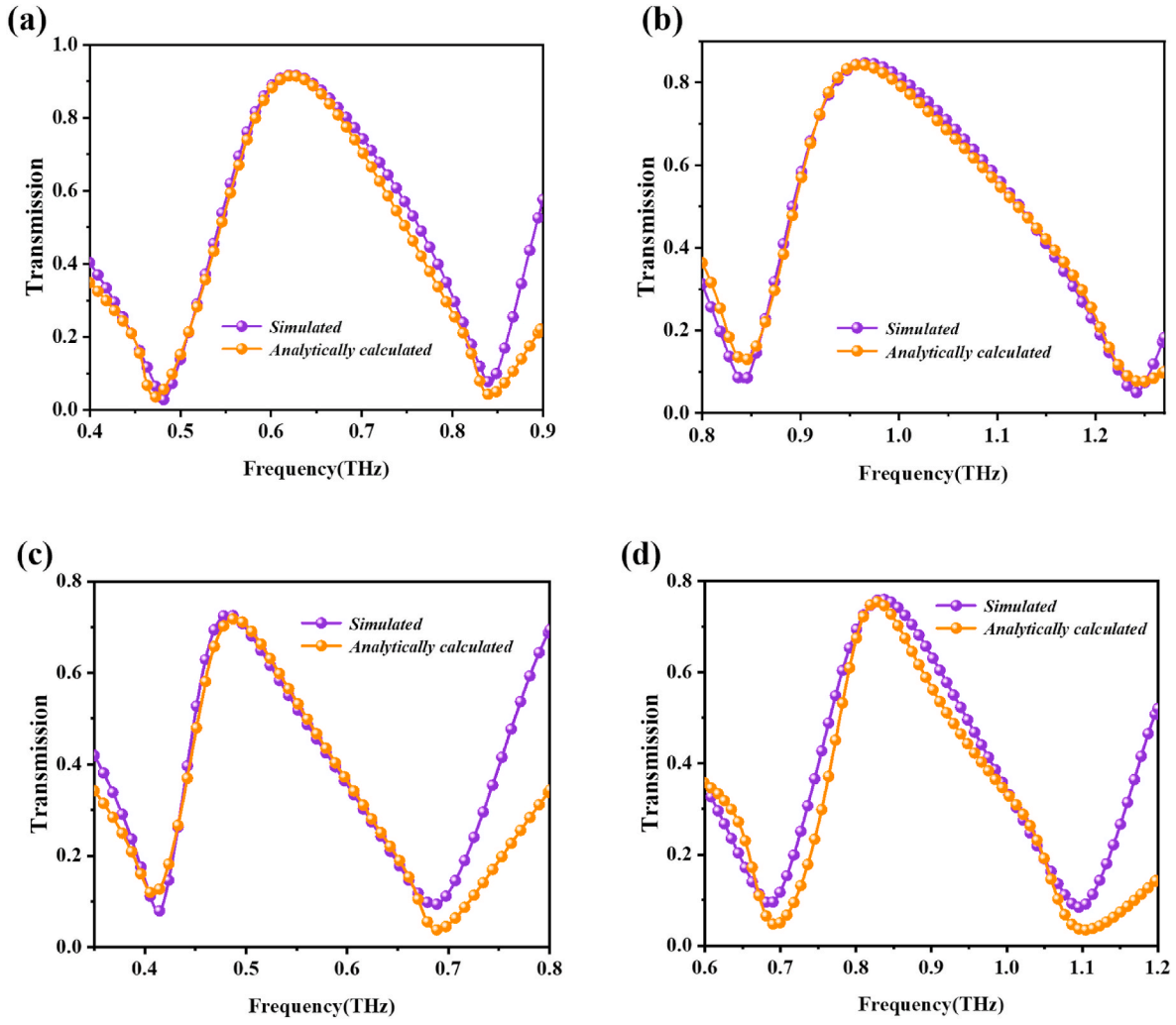


**Fig. 20.** The comparison of the simulated and analytically calculated curves of oscillator model of a) the first window in state 1, b) the second window in state 1, c) the first window in state 2 and d) the window peak in state 2.

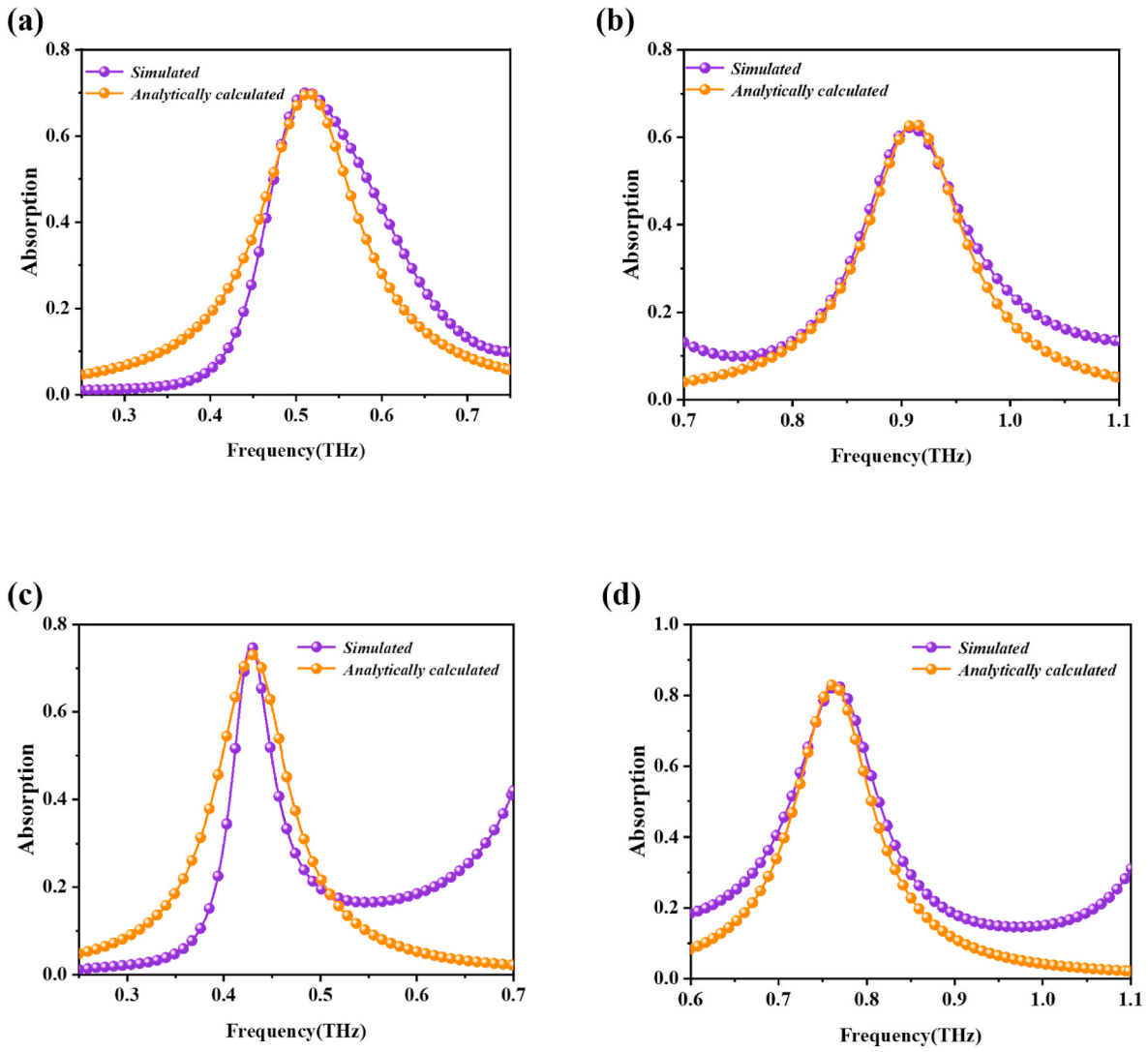


**Fig. 21.** The comparisons between the EIA absorption curves by simulation analysis (the purple traces) and analytical calculations (the orange traces) (a) for the first peak in state 3, (b) for the second peak in state 3, (c) for the first peak in state 4 and (d) for the second peak in state 4.

parameters are: $\omega_0 = 2.70$, $k = 0.104$, $\gamma_1 = 0.61$, $\gamma_2 = 0.60$ in the first window and $\omega_0 = 4.80$, $k = 0.104$, $\gamma_1 = 0.70$, $\gamma_2 = 0.60$ in the second window. The analytically derived transmission traces are depicted in Fig. 21, compared with the simulation results.

Tolerable errors can be attributed to the transmission loss and the iteration numbers with taking approximations. Overall, the established dual-vibrators system reproduces the EITs and EIAs validly, elaborating inside physical mechanisms equivalent to the role of a three-oscillator model and verifying the feasibility of the system in a more convenient way.

## 4. The discussion of crucial parameters in MS

To further investigate the influences of the parameters of the MS on the dual-peak EIT and EIA, the length of the $VO_2$ branches of CR2 and the radius of CR2 are selected for discussion and analysis in Figs. 22–23. Fig. 22 clearly shows the absorption curves under the incidence of CP waves in State 4 when $t_3$ varies equidistantly from 2 μm to 17 μm. It is strongly distinct that the first peak of EIA in State 4 is red-shifted and the second peak becomes stable as the values of $t_3$ increase. When $t_3 = 2$ μm, although the absorption dips are below 0.15, the peak frequency of State 3 and the valley frequency of State 4 have a large deviation at this time, which has an impact on the amplitude encoding effect in absorption

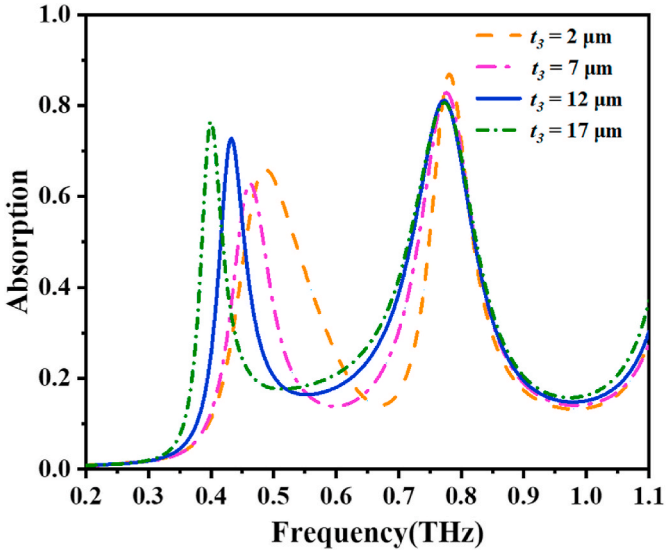


**Fig. 22.** The absorption curves of dual-peak EIA in State 4 under the discussion of the length of branches of CR2 $t_3$ ranging from 2 μm to 17 μm.

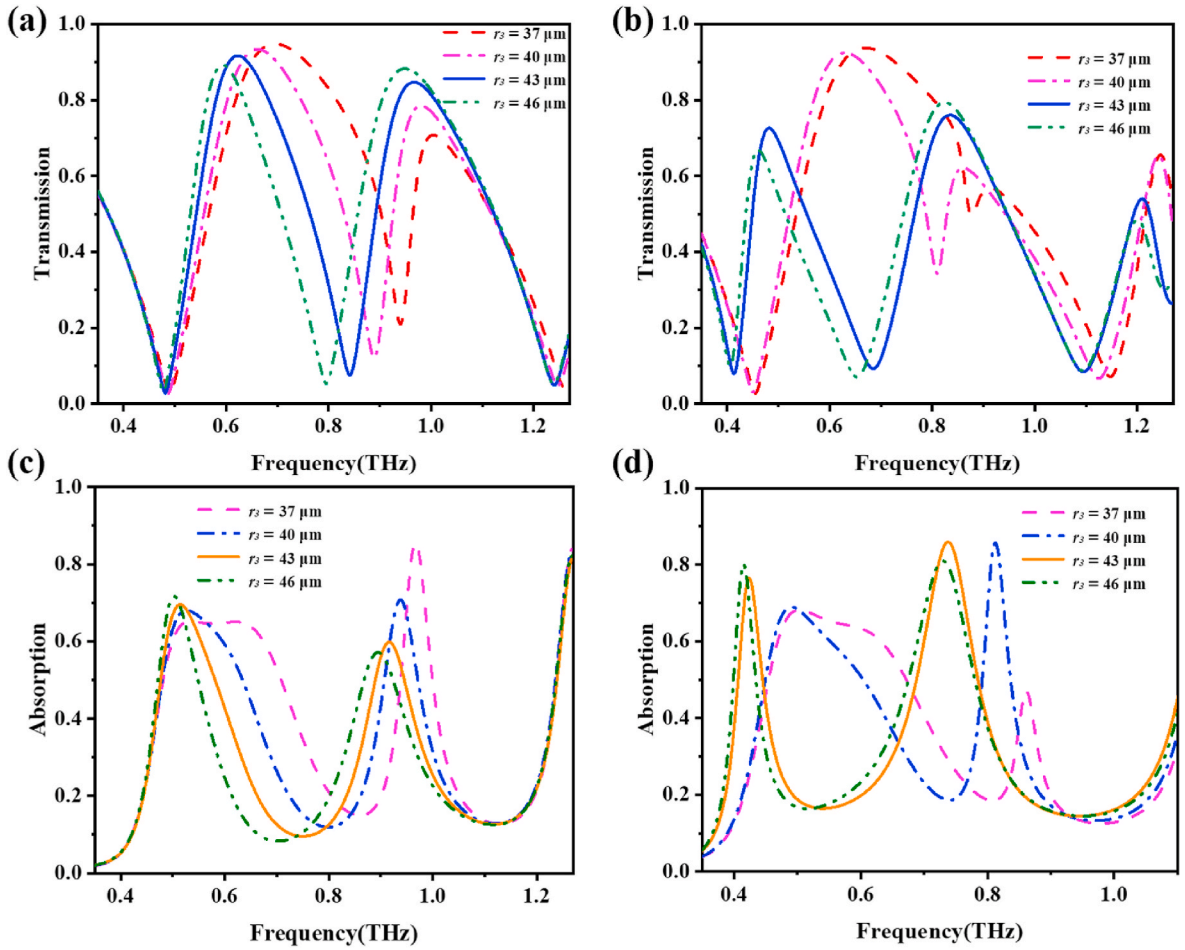


**Fig. 23.** The effects of the key parameters $r_3$ ranging from 37 μm to 46 μm a) in State 1, b) in State 2, c) in State 3 and d) in State 4.

states. When $t_3 = 7$ μm, the peak on the left side of the absorption curve cannot reach the optimum, while the peak and valley work very well at $t_3 = 12$ μm. However, once $t_3$ reaches 17 μm, although the peak value is good, the values of absorption dips in the middle exceed 0.15, so it is not selected. As a result, we chose the case of $t_3 = 12$ μm.

Fig. 23 shows the transparency and absorption curves under different values of $r_3$ in four states. As the increasing of $r_3$, the curves have undergone a significant red-shift whether in transparency states or absorption states. Once $r_3$ reaches 43 μm, the curves become stable. It is obvious from Fig. 23 that the transmission dips are all higher than 0.2 and the dual-peak EIAs are not well-formed when $r_3 = 37$ μm and 40 μm. Whereby, it is not available when $r_3 \leq 40$ μm. Furthermore, the effects of transmission response and absorption response are both worthy of adoption with $r_3 = 43$ μm and 46 μm. Nevertheless, when $r_3 = 43$ μm, the peak frequencies in one transparency/absorption state can be well aligned with the dip frequencies in the other state. So, to sum up, $r_3 = 43$ μm is the best choice.

## 5. Conclusion

In conclusion, the proposed polarization-insensitive MS is formed by combining three metal ring resonators with $VO_2$ branches and Si resonators. It is theoretically demonstrated that four states can be achieved by switching the metallic and insulating states of the phase change material $VO_2$ and the photosensitive material Si. When no pump light is irradiated, Si is insulating, indicating that the structure is in a transparent state. When $VO_2$ is insulating, the given MS is in State 1, which reveals that two transparent windows can be realized in the frequency band of 0.482–1.239 THz and the peaks at 0.622 THz and 0.964 THz can reach 0.917 and 0.847, respectively. Once $n = 300{,}000$ S/m (State 2), $VO_2$ branches will transform into a metallic state, which changes the resonance position of the original resonators. Hence, State 2 can be achieved in the range of 0.414–1.091 THz and the peaks at 0.482 THz and 0.835 THz can reach 0.728 and 0.760. Once the pump light is irradiated, $k$ has arrived at 500,000 S/m. Two transparency states can be successfully transformed into corresponding absorption states. When $n = 10$ S/m, two absorption windows can be formed between 0.35 THz and 1.11 THz accompanied by the peaks coming to 0.701 at 0.511 THz and 0.622 at 0.910 THz. Similarly, the absorption peaks are 0.749 and 0.830 at 0.429 THz and 0.764 THz in the frequency band between 0.35 THz and 0.96 THz. Besides, the four EIT windows of the two transparency states correspond to the four GDs: 2.59 ps, 3.16 ps, 4.13 ps, and 2.52 ps. Due to the variable nature of the group velocity, the proposed MS has broad application in the field of slow-light devices. Additionally, the oscillator model and the circuit model of EIT and EIA are utilized to theoretically fit the results to verify the correctness and feasibility of the MS.

## Credit author statement

You Lv, and Hai-Feng Zhang contributed to the novel idea of the study; Di-Di Zhu, Tian-Qi Zhu,Jian-Yu Gong contributed significantly to analysis and manuscript preparation; Hai-Feng Zhang performed the data analyses and wrote the manuscript.

## Declaration of competing interest

The authors declare that they have no known competing financial

interests or personal relationships that could have appeared to influence the work reported in this paper.

## Data availability

Data will be made available on request.

## Acknowledgment

This work was supported by the College Student Innovation Training Program of Nanjing University of Posts and Telecommunications.

## References

[1] Y.Z. Sun, D. Zhang, H.F. Zhang, Tailoring dual-band electromagnetically induced transparency with polarization conversions in a dielectric-metal hybrid metastructure, Opt Express 30 (2022) 30574–30591.
[2] Y. Tian, X.F. Jing, H. Yu, H.Y. Gan, C.X. Li, Z. Hong, Manipulation of the arbitrary scattering angle based on all-dielectric transmissive Pancharatnam Berry phase coding metasurfaces in the visible range, Opt Express 28 (2020) 32107–32123.
[3] V.C. Su, C.H. Chu, G. Sun, D.P. Tsai, Dvances in optical metasurfaces: fabrication and applications, Opt Express 26 (2018) 13148–13182.
[4] E. Distante, P. Farrera, A. Padrón-Brito, Storing single photons emitted by a quantum memory on a highly excited Rydberg state, Nat. Commun. 8 (1) (2017), 14072.
[5] B. Wu, J. Hulbert, E. Lunt, Slow light on a chip via atomic quantum state control, Nat. Photonics 4 (11) (2010) 776–779.
[6] M. Lukin, A. Imamoğlu, Controlling photons using electromagnetically induced transparency, Nature 413 (6853) (2001) 273–276.
[7] L. Wang, A. Fallahi, K. Ravi, F. Kärtner, High efficiency terahertz generation in a multi-stage system, Opt Express 26 (2018) 29744–29768.
[8] C.H. He, Z.Y. Song, Terahertz graphene metasurfaces for cross-polarized deflection, focusing, and orbital angular momentum, Opt Express 30 (14) (2022) 25498–25508.
[9] Z.K. Zhou, Z.Y. Song, Terahertz mode switching of spin reflection and vortex beams based on graphene metasurfaces, Opt Laser. Technol. 153 (2022), 108278.
[10] A. Markelz, A. Roitberg, E.J. Heilweil, Pulsed terahertz spectroscopy of DNA, bovine serum albumin and collagen between 0.1 and 2.0 THz, Chem. Phys. Lett. 320 (2000) 42–48.
[11] M. Nagel, P. Haring Bolivar, M. Brucherseifer, H. Kurz, A. Bosserhoff, R. Büttner, Integrated THz technology for label-free genetic diagnostics, Appl. Phys. Lett. 80 (2002) 154–156.
[12] K. Young, Q. Wen, S. Hanany, H. Imada, J. Koch, T. Matsumura, O. Suttmann, V. Schütz, Broadband millimeter-wave anti-reflection coatings on silicon using pyramidal sub-wavelength structures, J. Appl. Phys. 121 (2017), 213103.
[13] T. Kubacka, J. Johnson, M. Hoffmann, C. Vicario, S. de Jong, P. Beaud, S. Grübel, S.-W. Huang, L. Huber, L. Patthey, Y.-D. Chuang, J.J. Turner, G.L. Dakovski, W.-S. Lee, M.P. Minitti, W. Schlotter, R.G. Moore, C.P. Hauri, S.M. Koohpayeh, V. Scagnoli, G. Ingold, S.L. Johnson, U. Staub, Large-amplitude spin dynamics driven by a THz pulse in resonance with an electromagnon, Science 343 (2014) 1333–1336.
[14] T. Kampfrath, A. Sell, G. Klatt, A. Pashkin, S. Mährlein, T. Dekorsy, M. Wolf, M. Fiebig, A. Leitenstorfer, R. Huber, Coherent terahertz control of antiferromagnetic spin waves, Nat. Photonics 5 (2011) 31–34.
[15] M.S. Islam, J. Sultana, A. Dinovitser, B.W.-H. Ng, D. Abbot, Zeonex based asymmetrical terahertz photonic crystal fifiber for multichannel communication and polarization maintaining applications, Appl. Opt. 57 (4) (2018) 666–672.
[16] K.J. Boller, A. Imamoğlu, S.E. Harris, Observation of electromagnetically induced transparency, Phys. Rev. Lett. 66 (20) (1991) 2593–2596.
[17] S. Zhang, D.A. Genov, Y. Wang, et al., Plasmon-Induced transparency in metamaterials, Phys. Rev. Lett. 101 (4) (2008).
[18] S.E. Harris, J.E. Field, A. Imamoglu, Nonlinear optical processes using electromagnetically induced transparency, Phys. Rev. Lett. 64 (10) (1990) 1107–1110.
[19] K. Totsuka, N. Kobayashi, M. Tomita, Slow light in coupled-resonator-induced transparency, Phys. Rev. Lett. 98 (21) (2007), 213904.
[20] T. Baba, Slow light in photonic crystals, Nat. Photonics 2 (8) (2008) 465–473.
[21] R. Singh, C. Rockstuhl, F. Lederer, W. Zhang, Coupling between a dark and a bright eigenmode in a terahertz metamaterial, Phys. Rev. B 79 (2009), 085111.
[22] Y. Lu, J.Y. Rhee, W.H. Jang, Y.P. Lee, Active manipulation of plasmonic electromagnetically-induced transparency based on magnetic plasmon resonance, Opt Express 18 (2010), 20912.
[23] Q. Bai, C. Liu, J. Chen, C. Cheng, M. Kang, H.T. Wang, Tunable slow light in semiconductor metamaterial in a broad terahertz regime, J. Appl. Phys. 107 (2010), 093104.
[24] X. Ri Jin, J. Park, H.Y. Zheng, S.J. Lee, Y.P. Lee, J.Y. Rhee, K.W. Kim, H.S. Cheong, W.H. Jang, Highly-dispersive transparency at optical frequencies in planar metamaterials based on two-bright-mode coupling, Opt Express 19 (2011) 21652–21657.
[25] Z. Li, Y. Ma, R. Huang, R. Singh, J. Gu, Z. Tian, J. Han, W. Zhang, Manipulating the plasmon-induced transparency in terahertz metamaterials, Opt Express 19 (2011) 8912.
[26] J. Kim, R. Soref, W.R. Buchwald, Multi-peak electromagnetically induced transparency (EIT)-like transmission from bull's-eye-shaped metamaterial, Opt Express 18 (2010) 17997–18002.
[27] L. Zhu, H.D. Li, L. Dong, W.J. Zhou, M.X. Rong, X.Z. Zhang, J. Guo, Dual-band electromagnetically induced transparency (EIT) terahertz metamaterial sensor, Opt. Mater. Express 11 (2021) 2109–2121.
[28] K. Zhang, C. Wang, L. Qin, R.W. Peng, D.H. Xu, X. Xiong, M. Wang, Dual-mode electromagnetically induced transparency and slow light in a terahertz metamaterial, Opt Lett. 39 (12) (2014).
[29] A. Lezama, A.M. Akulshin, S. Barreiro, Electromagnetically induced absorption, Phys. Rev. 59 (6) (1999).
[30] Y. Sun, W. Tan, L. Liang, H.T. Jiang, Z.G. Wang, F.Q. Liu, H. Chen, Metamaterial analog of quantum interference: from electromagnetically induced transparency to absorption, EPL 98 (6) (2012).
[31] P. Tassin, L. Zhang, R. Zhao, A. Jain, T. Koschny, C.M. Soukoulis, Electromagnetically induced transparency and absorption in metamaterials: the radiating two-oscillator model and its experimental confirmation, Phys. Rev. Lett. 109 (18) (2012), 187401.
[32] X.Q. Zhang, N.N. Xu, K.N. Qu, Z. Tian, R.J. Singh, J.G. Han, G.S. Agarwal, W. L. Zhang, Electromagnetically induced absorption in a three-resonator metasurface system, Sci. Rep. 5 (1) (2015).
[33] J. Vanier, Atomic clocks based on coherent population trapping: a review, Appl. Phys. B 81 (4) (2005) 421–442.
[34] D. Budker, M.V. Romalis, Optical magnetometry, Nat. Phys. 3 (4) (2007) 227–234.
[35] L.V. Hau, S.E. Harris, Z. Dutton, C.H. Behroozi, Light sped reduction to 17 meters per second in an ultracold atomic gas, Nature 397 (6720) (1999) 594–598.
[36] I.H. Bae, H.S. Moon, Continuous manipulation of light group velocity from subluminal to superluminal with a standing-wave coupling field in an Rb vapor cell, Phys. Rev. 83 (2011), 053806.
[37] M.P. Hokmabadi, J.H. Kim, E. Rivera, P. Kung, S.M. Kim, Impact of substrate and bright resonances on group velocity in metamaterial without dark resonator, Sci. Rep. 5 (2015), 14373.
[38] T. Matsui, M. Liu, D.A. Powell, I.V. Shadrivov, Y.S. Kivshar, Electromagnetic tuning of resonant transmission in magnetoelastic metamaterials, Appl. Phys. Lett. 104 (16) (2014), 161117.
[39] J.B. Pendry, D. Schurig, D.R. Smith, Controlling electromagnetic fields, Science 312 (5781) (2006).
[40] D. Schurig, J.J. Mock, B.J. Justice, S.A. Cummer, J.B. Pendry, A.F. Starr, D. R. Smith, Metamaterial electromagnetic cloak at microwave frequencies, Science 314 (5801) (2006).
[41] T. Ergin, N. Stenger, P. Brenner, J.B. Pendry, M. Wegener, Three-dimensional invisibility cloak at optical wavelengths, Science 328 (5976) (2010).
[42] J.B. Pendry, Negative refraction makes a perfect lens, Phys. Rev. Lett. 85 (18) (2000).
[43] N. Fang, H. Lee, C. Sun, X. Zhang, Sub-diffraction-limited optical imaging with a silver superlens, Science 308 (5721) (2005).
[44] Q. Wang, E. Plum, Q.L. Yang, X.Q. Zhang, Q. Xu, Y.H. Xu, J.G. Han, W.L. Zhang, Reflective chiral meta-holography: multiplexing holograms for circularly polarized waves, Light Sci. Appl. 7 (1) (2018).
[45] W.W. Liu, J.S. Xu, Z.Y. Song, Bifunctional terahertz modulator for beam steering and broadband absorption based on a hybrid structure of graphene and vanadium dioxide, Opt Express 29 (15) (2021) 23331–23340.
[46] C.Q. Li, Z.Y. Song, Tailoring terahertz wavefront with state switching in VO2 Pancharatnam–Berry metasurfaces, Opt Laser. Technol. 157 (2023), 108764.
[47] R.X. Nie, C.H. He, R.X. Zhang, Z.Y. Song, Vanadium dioxide-based terahertz metasurfaces for manipulating wavefronts with switchable polarization, Opt Laser. Technol. 159 (2023), 109010.
[48] Y.J. Zhao, R.C. Yang, Y.X. Wang, W.M. Zhang, J.P. Tian, $VO_2$-assisted multifunctional metamaterial for polarization conversion and asymmetric transmission, Opt Express 30 (15) (2022) 27407–27417.
[49] Y. Ren, B. Tang, Switchable multi-functional $VO_2$-integrated metamaterial devices in the terahertz region, J. Lightwave Technol. (2021) 5864–5868.
[50] Z. Song, A. Chen, J. Zhang, Terahertz switching between broadband absorption and narrowband absorption, Opt Express 28 (2) (2020) 2037–2044.
[51] T.L. Wang, H.Y. Zhang, Y. Zhang, Y.P. Zhang, M.Y. Cao, Tunable bifunctional terahertz metamaterial device based on Dirac semimetals and vanadium dioxide, Opt Express 28 (12) (2020) 17434–17448.
[52] Z.Y. Song, A.P. Chen, J.H. Zhang, J.Y. Wang, Integrated metamaterial with functionalities of absorption and electromagnetically induced transparency, Opt Express 27 (2019) 25196–25204.
[53] J.Y. Wang, R.C. Yang, Z. H L, J.P. Tian, Reconfigurable multifunctional polarization converter based on asymmetric hybridized metasurfaces, Opt. Mater. 124 (2022), 111953.
[54] Z. H L, R.C. Yan, J.Y. Wan, Y.J. Zhao, J.P. Tian, W.M. Zhang, Multifunctional metasurface for broadband absorption, linear and circular polarization conversions, Opt. Mater. Express 11 (10) (2021) 3507–3519.
[55] S. Yuan, R.C. Yang, J.P. Tian, W.M. Zhang, A Photoexcited Switchable Tristate Terahertz Metamaterial Absorber, International Journal of RF and Microwave Computer-Aided Engineering, 2019.
[56] Y.Z. Cheng, R.Z. Gong, J.C. Zhao, A photoexcited switchable perfect metamaterial absorber/reflector with polarization-independent and wide-angle for terahertz waves, Opt. Mater. (2016) 62.
[57] Y.Z. Cheng, R.Z. Gong, Z.Z. Cheng, A photoexcited broadband switchable metamaterial absorber with polarization-insensitive and wide-angle absorption for terahertz waves, Opt Commun. (2016) 361.

[58] Y.Z. Sun, Z.H. Guo, C.J. Gao, H.F. Zhang, Tunable polarization comb based on the electromagnetically induced transparency with hybrid metal-graphene metamaterial, Phys. Scripta 96 (12) (2021).
[59] M.Z. Lu, W.Z. Li, E.R. Brown, Second-order bandpass terahertz filter achieved by multilayer complementary metamaterial structures, Opt Lett. 36 (7) (2011).
[60] Z.Y. Shi, L.X. Song, T. Zhang, Optical and electrical characterization of pure PMMA for terahertz wide-band metamaterial absorbers, J. Infrared, Millim. Terahertz Waves 40 (1) (2019).
[61] B.H. Sohn, B.H. Seo, Fabrication of the multilayered nanostructure of alternating polymers and gold nanoparticles with thin films of self-assembling diblock copolymers, Chem. Mater. 13 (5) (2001) 1752–1757.
[62] H. Masa-aki, K. Katsuaki, T. Keiichi, Fabrication and functions of surface nanomaterials based on multilayered or nanoarrayed assembly of metal complexes [J], Coord. Chem. Rev. 251 (21) (2007).
[63] A. Jabbar, O. Siddiqui, F.A. Tahir, M. Amin, R. Ramzan, A Lumped Element Analog of Dual-Stub Microwave Electromagnetically Induced Transparency resonator." 2018 18th Mediterranean Microwave Symposium (MMS), IEEE, 2018, pp. 168–170.
[64] C.J. Ma, Y.B. Zhang, Y. Zhang, S.Q. Bao, J.S. Jin, M. Li, D.M. Li, Y.G. Liu, Y.P. Xu, All-optical tunable slow-light based on an analogue of electromagnetically induced transparency in a hybrid metamaterial, Nanoscale Adv. 3 (19) (2021).
[65] Q. Bai, C. Liu, J. Chen, C. Cheng, M. Kang, H.T. Wang, Tunable slow light in semiconductor metamaterial in a broad terahertz regime, J. Appl. Phys. 107 (9) (2010), 093104.
[66] Y.Z. Sun, C.J. Gao, J. Qu, H.F. Zhang, Circularly polarized manipulations with VO2-doped dielectric electromagnetically induced transparency and absorption, Ann. Phys. 534 (6) (2022), 2200130.
[67] R. Ramzan, M. Omar, O.F. Siddiqui, M. Amin, N. Bastaki, T.S. Ksiksi, Electromagnetically induced absorption in the near-field of microwave radiative elements with application to foliage moisture sensing, IEEE Access 6 (2018).
[68] M. Amin, R. Ramzan, O. Siddiqui, Slow wave applications of electromagnetically induced transparency in microstrip resonator, Sci. Rep. 8 (1) (2018) 2357.
[69] A. Bhattacharya, R. Sarkar, N.K. Sharma, Multiband transparency effect induced by toroidal excitation in a strongly coupled planar terahertz metamaterial, Sci. Rep. 11 (1) (2021), 19186.
[70] J.N. He, P. Ding, J.Q. Wang, C.Z. Fan, E.J. Liang, Ultra-narrow band perfect absorbers based on plasmonic analog of electromagnetically induced absorption, Opt Express 23 (5) (2015) 6083–6091.
[71] R. Taubert, M. Hentschel, H. Giessen, Plasmonic analog of electromagnetically induced absorption: simulations, experiments, and coupled oscillator analysis, JOSA B 30 (12) (2013) 3123–3134.